catalysts

MDPI

Review

g-C_3N_4-Based Heterojunction for Enhanced Photocatalytic Performance: A Review of Fabrications, Applications, and Perspectives

Junxiang Pei, Haofeng Li, Dechao Yu * and Dawei Zhang

Engineering Research Center of Optical Instrument and System, Ministry of Education and Shanghai Key Lab of Modern Optical System, University of Shanghai for Science and Technology, Shanghai 200093, China; jxpei@usst.edu.cn (J.P.); lhf09042023@163.com (H.L.); dwzhang@usst.edu.cn (D.Z.)
* Correspondence: d.yu@usst.edu.cn

Abstract: In recent years, photocatalysts have attracted wide attention in alleviating energy problems and environmental governance, among which, g-C_3N_4, as an ideal photocatalyst, has shown excellent application potential in achieving the sustainable development of energy. However, its photocatalytic performance needs to be further improved in some applications. Rational construction of heterostructures with two or more semiconductor materials can combine the advantages of multi-components to simultaneously improve the photo-induced charge separation, which is very conducive to improving the absorption of visible light and obtaining more efficient redox capacity. With the rapid development in photocatalysis of g-C_3N_4-based heterostructures, a systematic summary and prospection of performance improvement are urgent and meaningful. This review focuses on various kinds of effective methods of heterogeneous combination; as well, strategies for improving the photocatalytic performance are fully discussed. In addition, the applications in efficient photocatalytic hydrogen production, photocatalytic carbon dioxide reduction, and organic pollutant degradation are systematically demonstrated. Finally, the remaining issues and prospects of further development are proposed as a kind of guidance for g-C_3N_4-based heterostructures with high efficiency at photocatalysis.

Keywords: g-C_3N_4; heterojunction; fabrications; mechanism; photocatalytic

Citation: Pei, J.; Li, H.; Yu, D.; Zhang, D. g-C_3N_4-Based Heterojunction for Enhanced Photocatalytic Performance: A Review of Fabrications, Applications, and Perspectives. *Catalysts* **2024**, *14*, 825. https://doi.org/10.3390/catal14110825

Academic Editor: Nina Kaneva

Received: 13 October 2024
Revised: 10 November 2024
Accepted: 14 November 2024
Published: 16 November 2024

1. Introduction

Nowadays, energy shortages and environmental pollution have become global problems. In order to ensure sustainable development and energy recycling, there is an urgent need to develop renewable energy and green technologies that promote the degradation of pollutants. Among them, semiconductor photocatalysis technology has great development potential in alleviating energy problems and controlling environmental pollution [1–7]. Semiconductor photocatalysis technology refers to the process of converting light energy into chemical energy and promoting the synthesis or degradation of organic matter under the irradiation of light [8–10]. Generally speaking, photocatalytic reactions mainly include three reaction processes: (1) when the photon energy of the incident semiconductor nanoparticle is greater than or equal to the semiconductor band gap energy, photogenerated electron hole pairs are generated; (2) photogenerated electrons and holes are captured by vacancy defects or hanging bonds in the semiconductor material and then diffused to the surface of the semiconductor nanoparticles; (3) the photogenerated electrons and holes on the semiconductor surface adsorb materials on the catalyst surface and undergo redox reactions with them. It can be seen that improving the process parameters of the above three reaction processes plays an important role in improving the photocatalytic efficiency. However, at present, most of the photocatalytic reaction systems mainly use heavy metal atoms as catalysts, which leads to the high cost of the whole photocatalytic system and serious toxic pollution in the post-treatment process.

Graphite carbon nitride (g-C_3N_4) is a metal-free conjugated semiconductor with triazine or heptazine as a basic structural unit, and has a graphite-like layer structure [11–13]. Due to the hybridization of C and N atoms in g-C_3N_4 forming highly delocalized conjugates, g-C_3N_4 exhibits high thermal and chemical stability, making it an ideal candidate for photocatalysis: it has good physicochemical stability, nontoxicity, an applicable bandgap energy of about 2.7 eV with visible light absorption, and a composition of earth-abundant elements [14–16]. Studies have shown that solar-driven g-C_3N_4 photocatalysts can be used to decompose water to produce hydrogen, degrade organic pollutants, reduce CO_2 to organic fuels, or convert solar energy into other forms of energy [12,17–29]. However, with the increasing demand for photocatalytic efficiency in industrial development, g-C_3N_4 inevitably presents some problems that limit its feasibility as an efficient photocatalyst. The main deficiencies of g-C_3N_4 are (1) photoexcited recombination, (2) poor visible light absorption, (3) easy poisoning by the produced H_2O_2, (4) limited specific surface area, and (5) low intrinsic quantum efficiency. To solve these problems in the application of g-C_3N_4 in photocatalysis, researchers have improved the photocatalytic efficiency of g-C_3N_4 by adjusting various process parameters, such as morphological regulation, element doping, precious metal deposition, and heterogeneous structure construction. However, studies have shown that it is difficult for a single component catalyst to have a wide light absorption spectrum, fast charge separation, and strong redox ability at the same time [30–37]. Therefore, building g-C_3N_4-based heterostructures or preparing composite materials is an effective way to solve the subsistent issues.

Although several review articles have summarized and discussed the performance of g-C_3N_4 base heterojunctions, usually only one application or one class of heterojunctions has been discussed in detail [38–40]. The novelty of this review is starting from the different synthesis methods of g-C_3N_4, and then comprehensively and systematically summarizing almost all components that can form heterojunctions with g-C_3N_4 and their structural types. In this review, the fabrications and the applications of g-C_3N_4-based heterostructure photocatalysts are carefully reviewed. The overall framework of g-C_3N_4 and g-C_3N_4-based heterojunctions for enhanced photocatalytic performance are displayed in Figure 1. The various synthesis methods of g-C_3N_4 and g-C_3N_4-based heterojunctions are firstly reviewed, which provides comprehensive understanding of the strategies for constructing g-C_3N_4-based heterostructures with high photocatalytic efficiency. Subsequently, the structure design and energy band design of g-C_3N_4-based heterojunction photocatalysts are introduced. The factors and mechanisms affecting the separation and transfer of photogenerated electron hole pairs in g-C_3N_4-based heterojunction photocatalysts are discussed. The application of g-C_3N_4-based heterojunction photocatalytic systems in hydrogen evolution, CO_2 reduction, degradation of organic pollutants, and biomedicine is summarized and analyzed. Finally, constructive suggestions are put forward for future research improvements and expectations in g-C_3N_4-based heterogeneous photocatalysts. This review has certain reference value for the design and preparation of g-C_3N_4-based heterojunction photocatalysts with high photocatalytic efficiency.

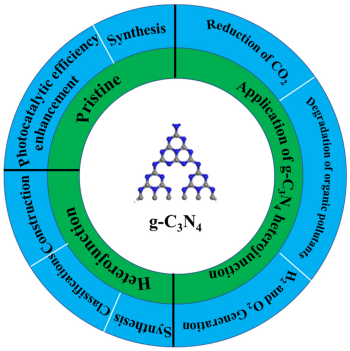

Figure 1. Overall framework of g-C_3N_4 and g-C_3N_4-based heterojunction for enhanced photocatalytic performance.

2. Synthesis

2.1. Synthesis of g-C_3N_4

Typically, triazine (C_3N_3) or tri-s-triazine (C_6N_7) are the building blocks of g-C_3N_4, as shown in Figure 2a,b. According to the arrangement order or structure, g-C_3N_4 can be divided into five crystalline phases, namely, α-phase, β-phase, c-phase, p-phase and g-phase [41–43]. g-C_3N_4 has been demonstrated to have excellent thermal and chemical stability [44]. The C and N atoms are present in the structure of g-C_3N_4 in the form of sp^2 hybridized distributions [35,45,46]. The application of g-C_3N_4 as a heterogeneous catalyst was first reported by Frederic Goettmann in 2006 [47]. Subsequently, more and more research on the application of g-C_3N_4 for photocatalysis was reported. In these studies, g-C_3N_4 was generally fabricated simply through thermal treatment of abundant nitrogenous substrates, such as urea, thiourea, melamine, cyanamide, dicyandiamide, guanidinium chloride, guanidine thiocyanate, and so forth [48,49]. The surface area of g-C_3N_4 prepared via one-step heating is usually small (normally below 10 m^2 g^{-1}). However, the size of the surface area will directly affect the catalytic efficiency of g-C_3N_4. Therefore, it is very important to improve the synthesis method to effectively increase the surface area and active site of g-C_3N_4. The lamellar structures have advanced photocatalytic performance, giving rise to intriguing surface, optical, and electronic properties. As shown in Figure 2c–f, various kinds of feasible methods to exfoliate g-C_3N_4 are proposed, including sonication-assisted liquid exfoliation, liquid ammonia-assisted lithiation, acid/base-assisted stripping, post-thermal oxidation etching, and integrated thermal delamination with an ultrasonication process [47,50–56]. Nano-template or nano-casting technology is a kind of nano-scale preparation process, which can effectively regulate the interlayer interaction and structure. This method can be used to characterize the void fraction in g-C_3N_4. In addition, the morphology, specific surface area, porosity, and size of g-C_3N_4 can be flexibly adjusted by various processes, such as the soft and hard template method and supramolecular pre-organization method [57–62]. Soft template strategies usually require the adoption of organic substances such as surfactants as templates [63–65]. The commonly used materials for hard templates are mainly mesoporous silica, alumina, and nano calcium carbonate [66,67].

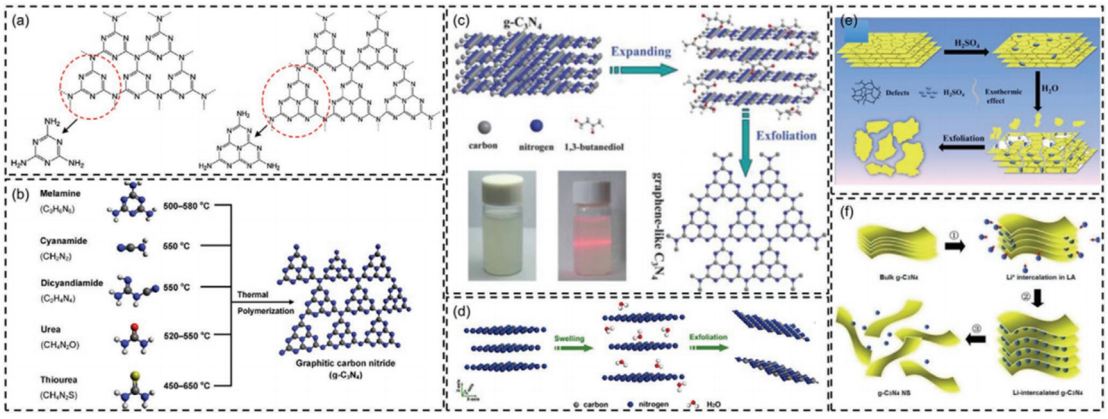

Figure 2. Schematic illustration of structures and synthesis methods of g-C_3N_4. (**a**) The structural motif of triazine and tri-s-triazine (heptazine) in g-C_3N_4. (**b**) Thermal polymerization of various precursors for bulk g-C_3N_4 preparation. (**c**,**d**) Sonication-assisted organic aqueous liquid-exfoliation process of bulk g-C_3N_4. Reproduced with permission [51,55]. (**e**) Acid-assisted stripping process of bulk g-C_3N_4 [53]. (**f**) Liquid ammonia-assisted lithiation and exfoliation of bulk g-C_3N_4 [52].

2.2. Synthesis of g-C_3N_4-Based Heterojunction

2.2.1. Photocatalytic Efficiency Enhancement of g-C_3N_4-Based Heterojunction

Before discussing the synthesis methods of g-C_3N_4-based heterojunction, it is essential to clarify the electron transport process and photocatalytic efficiency enhancement mechanism of g-C_3N_4-based heterojunction.

When the energy of the incident photon is greater than or equal to the band gap of g-C_3N_4, the electron hole pairs will be excited in g-C_3N_4. Subsequently, the photogenerated electron hole pairs are separated under bias and migrate to the surface of g-C_3N_4. When electrons and holes come into contact with reactants, a redox reaction occurs. It can be seen that the reaction site may occur on the surface of g-C_3N_4 or at the interface where it is in contact with another semiconductor or cocatalyst [68]. It is not difficult to see that the main role of g-C_3N_4 as a photocatalyst is to absorb light and produce electron hole pairs, and then migrate to its surface or cocatalyst. However, g-C_3N_4 is chemically active only when the photoinduced electron hole pair is consumed simultaneously before the recombination occurs in a fraction of a nanosecond [69–71].

The schematic illustration of photoexcited electron–hole pairs in g-C_3N_4 with a possible decay pathway is displayed in Figure 3. Notably, the migration of electrons and holes to the catalyzed substance forms the reduction and oxidation processes (pathways 1 and 2), but also competes with the carrier recombination process [72]. In general, the recombination process involves two main approaches: (1) on the surface of particle depicted in pathway 3 (surface recombination), and (2) in the bulk of g-C_3N_4 illustrated in pathway 4 (volume recombination). In fact, the recombination process is one of the important factors that inhibits the efficiency of photocatalysis. When the carrier recombination occurs, that is, when the excited electron returns to the valence band to recombine with the hole, the energy dissipates in the form of heat. This process prevents the carrier from participating in the redox reaction with the adsorbent on the surface of g-C_3N_4 [73]. Therefore, various strategies are employed to increase the carrier lifetime of g-C_3N_4 and thus improve photocatalytic performance. Especially, the construction of g-C_3N_4-based heterojunction nanohybrids has elicited a lot of attention in the field of photocatalysis, which will be comprehensively reviewed in the following sections.

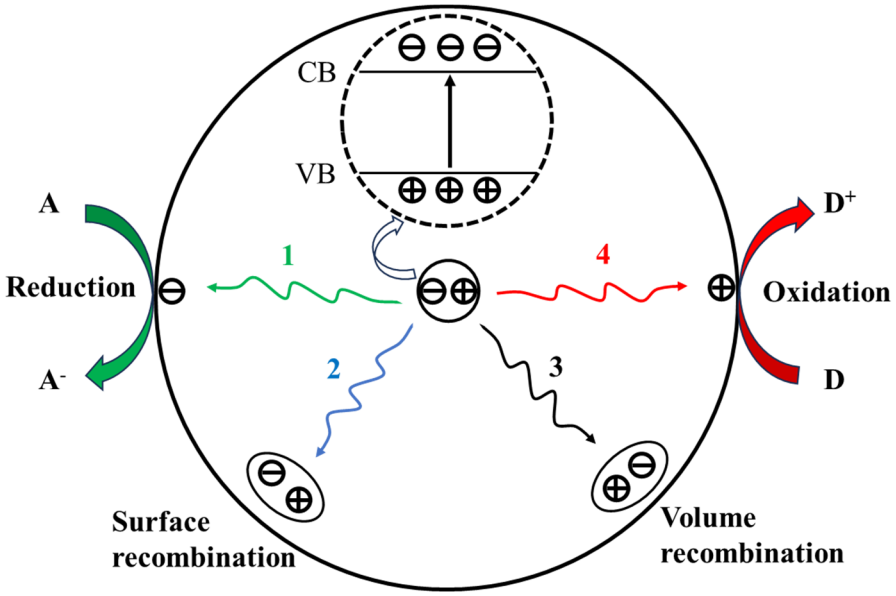

Figure 3. Schematic illustration of photoexcited electron hole pairs in g-C_3N_4 with possible decay pathway. A: electron acceptor; D: electron donor.

Typically, g-C_3N_4-based heterojunction photocatalysts are composed of g-C_3N_4 and another semiconductor material, mainly taking advantage of the photoelectric semiconductor properties of both materials. In order to broaden the spectrum absorption range, the band gap of the g-C_3N_4-based heterojunction is usually narrower compared to those of g-C_3N_4 photocatalysts [74]. The potential difference between the two sides results in band bending at the interface of the heterojunction nanocomposites, which induces a built-in electric field within the space charge region, thus causing the photogenerated electrons and

holes to spatially separate and migrate [75]. According to the different charge transfer paths in the g-C_3N_4-based heterojunction, the coupled composites can be categorized into three classifications, i.e., type II, Z-scheme, and type S heterojunctions, as shown in Figure 4.

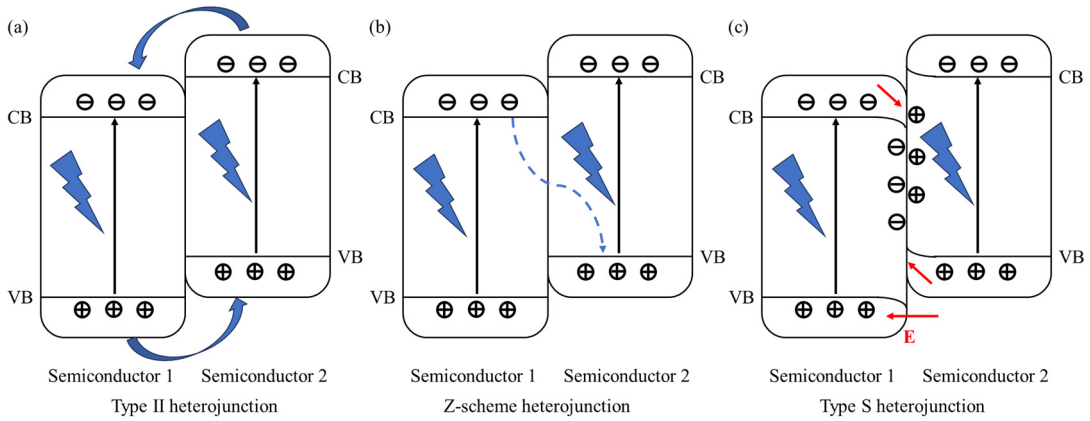

Figure 4. Different types of g-C_3N_4 heterojunction. (**a**) Type II. (**b**) Z-scheme. (**c**) Type-S.

In a type II heterojunction, the edge potential is staggered between semiconductor 1 and semiconductor 2. Due to the barrier height difference between the two semiconductors, an upward or downward band bending is formed, which in turn causes the carrier to migrate in the opposite direction. Therefore, this structural design can significantly enhance the spatial separation of electron hole pairs in heterojunctions, reduce charge recombination, and extend the lifetimes of free electrons and holes. When the type II heterojunction is excited by external light radiation, photoelectron–hole pairs will be generated in semiconductor 1 and semiconductor 2, and then the electrons on the conductor band of semiconductor 2 will be transferred to semiconductor 1. g-C_3N_4 has a conduction potential of −1.1 eV, which is more electronegative than most semiconductor catalysts. Therefore, when visible light is incident, the photoexcited electrons in its conduction band can quickly migrate to the conduction band of another semiconductor catalyst with a higher potential. At the same time, the transport path of the photoexcited hole is opposite to that of the photoexcited electron.

In the Z-scheme heterojunction, both semiconductors can produce electron–hole pairs under visible light. The electrons at the bottom of the conduction band of semiconductor 1 will be transferred to the top of the valence band of semiconductor 2 through the heterojunction and compound with the holes in the valence band. Therefore, the photogenerated holes and electrons with strong redox ability are retained in the valence band of semiconductor 1 and the conduction band of semiconductor 2, respectively. It is easy to see that the transfer path of Z-scheme heterojunction can not only improve the separation efficiency of photogenerated charge carriers, but also maintain the strong redox ability of photogenerated charge carriers, which is very beneficial to improve the photocatalytic efficiency.

It is worth mentioning that both semiconductors in the type S heterojunction are n-type semiconductors. They are composed of strong reducing photocatalyst and strong oxidizing photocatalyst. In type S heterojunctions, the built-in electric field, band bending, and coulomb interaction can effectively promote the separation of electron–hole pairs. The charge transfer mechanism of the type S heterostructure is shown in Figure 4c. It is not difficult to find that semiconductor 2 has higher conduction and valence band positions than semiconductor 1. When two semiconductors are in close contact to form a type S heterojunction, electrons will diffuse from the conduction band of semiconductor 2 to semiconductor 1, while forming a built-in electric field. This band bending facilitates recombination of electrons in semiconductor 1 with holes in semiconductor 2. Therefore, the type-S heterojunction not only retains the electron holes with high redox ability in

semiconductors 1 and 2, but also facilitates charge transfer and separation by the structure design of band bending.

2.2.2. Construction of Metal/g-C_3N_4 Heterojunctions

According to the literature, the construction of metal/g-C_3N_4 heterojunctions can effectively increase light absorption, reduce the band gap, accelerate charge migration, and prolong the carrier lifetime, all of which are necessary for significant photocatalytic activity. Cheng et al. synthesized Au nanoparticles (AuNP) on g-C_3N_4 nanosheets by ultrasonication-assisted liquid exfoliation as an effective photocatalyst [76]. Under visible light irradiation, g-C_3N_4 nanosheets and AuNP/g-C_3N_4 hybrid showed good photocatalytic degradation activity of methyl orange. The TEM image of the g-C_3N_4 nanosheets is displayed in Figure 5A–F, which demonstrated that the bulk g-C_3N_4 is successfully exfoliated into g-C_3N_4 nanosheets. As shown in Figure 5E, a large number of nanoparticles with diameters ranging from 5 to 20 nm were generated on the nanosheet under visible light irradiation. All these observations show the formation of AuNP-loaded g-C_3N_4 nanosheets. The mechanism of photocatalytic degradation of MO by AuNP/g-C_3N_4 heterojunction under visible light irradiation is shown in Figure 5G. Photogenerated electron–hole pairs (e^- and h^+) are generated in g-C_3N_4 nanosheets under visible light irradiation. The photogenerated electron reacts with O_2 in the photodegradation system and reduces it to superoxide anion O^{2-}. Subsequently, MO molecules are degraded by photogenerated h^+ and O^{2-}. The AuNPs can be used as an electron trap to improve the separation efficiency of photogenerated electron–hole pairs and the transfer efficiency of interface electrons. Therefore, compared with g-C_3N_4, g-C_3N_4 nanosheets, and AuNP/g-C_3N_4 heterojunctions, g-C_3N_4 heterojunctions can not only exhibit a higher specific surface area, but also effectively promote the separation of photogenerated electron–hole pairs, which is an effective strategy to improve the photocatalytic efficiency of g-C_3N_4.

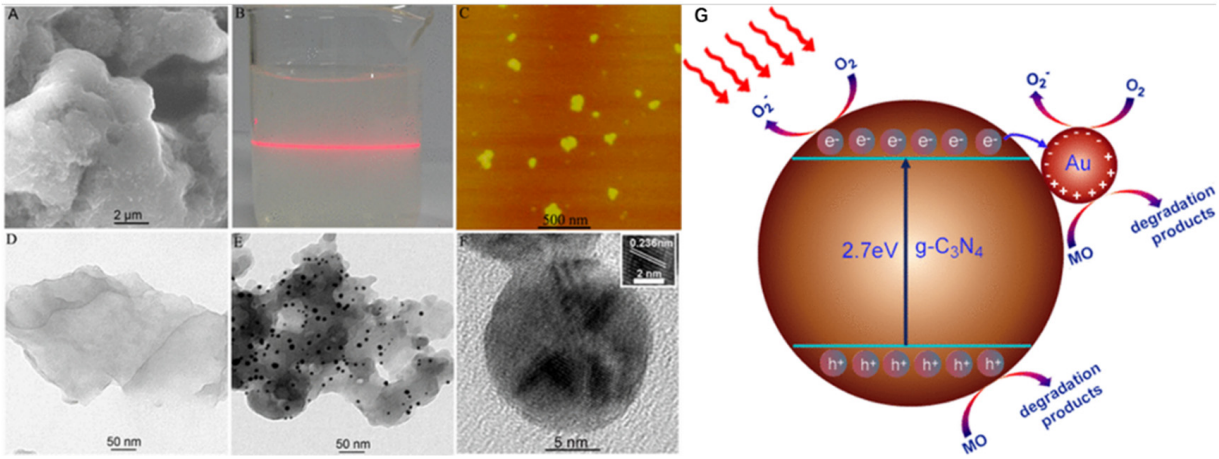

Figure 5. (**A**) SEM image of bulk g-C_3N_4. (**B**) Tyndall effect exhibited by aqueous dispersion of g-C_3N_4 nanosheets passed through with red laser light. (**C**) AFM and (**D**) TEM images of g-C_3N_4 nanosheets. (**E**) TEM image of AuNP/g-C_3N_4 nanohybrids. (**F**) High-magnification TEM image and corresponding HRTEM image (inset) of one single AuNP. (**G**) Schematic diagram illustrating the photocatalytic degradation of MO over AuNP/g-C_3N_4 nanohybrid under visible-light irradiation.

In addition, noble metals are also a material with excellent photoelectronic properties, which have attracted attention for photocatalytic applications. Recently, Yang et al. reported a Ru/g-C_3N_{4-x} heterojunction photocatalyst. This heterojunction is composed of small Ru NPs immobilized on g-C_3N_{4-x} nanosheets with nitrogen vacancy defects. The photoexcited electrons in g-C_3N_{4-x} promote the deposition of Ru NPs. The oxygen-free radicals generated by holes induce the formation of nitrogen vacancy defects on g-C_3N_{4-x} [77]. The specific preparation process is shown in Figure 6a. Firstly, an appropriate amount

of $NaIO_3$ is added to the aqueous suspension of g-C_3N_4 containing Ru^{3+}. Then, Ru/g-C_3N_{4-x} heterojunction photocatalysts with interfacial Ru and nitrogen-vacancy active sites were prepared by photoinduction. In the same way, N-deficient g-C_3N_4 (g-C_3N_{4-x}) was prepared without Ru^{3+} ions. g-C_3N_4 can produce electron–hole pairs under excitation light. The Ru^{3+} and IO^{3-} ions adsorbed on g-C_3N_4 nanosheets are electron acceptors, where Ru^{3+} ions will be electronically reduced to Ru NPs. The TEM image in Figure 6b shows that the nanoparticles on Ru/g-C_3N_{4-x} are about 2–4 nm. The HRTEM and EDS mapping are shown in Figure 6c,d; it can be seen that the lattice spacing (002) and (100) of Ru were tested as corresponding to 0.214 nm and 0.232 nm, respectively, which further confirmed the formation of small Ru NPs on the g-C_3N_4 nanosheet. The photocatalytic redox coupling reaction of H_2 evolution and benzyl alcohol oxidation is carried out in benzyl alcohol aqueous solution composed of 0.3 mL benzyl alcohol, 5 mg photocatalyst, and 30 mL deionized water, under simulated sunlight from a Xe lamp. In comparison, Ru/g-C_3N_{4-x} heterojunction photocatalyst exhibited a more efficient selective oxidation of benzyl alcohol. Furthermore, the reusability of Ru/g-C_3N_{4-x} photocatalyst is examined by performing the cyclic reactions in benzyl alcohol aqueous solution, with each cycle for 3 h. The activity and selectivity of Ru/g-C_3N_{4-x} photocatalysts are well maintained after four photocatalytic cycles, as shown in Figure 7a–e. Theoretical analysis and experimental results demonstrated that the synergistic effect of the interface Ru site and nitrogen vacancy defect on g-C_3N_{4-x} is an important factor to improve the efficiency of photocatalytic redox reaction. The modified Ru/g-C_3N_{4-x} heterojunction interface can not only promote the separation of photogenerated charge carriers, but also provide the best active site for hydrogen precipitation and benzyl alcohol oxidation.

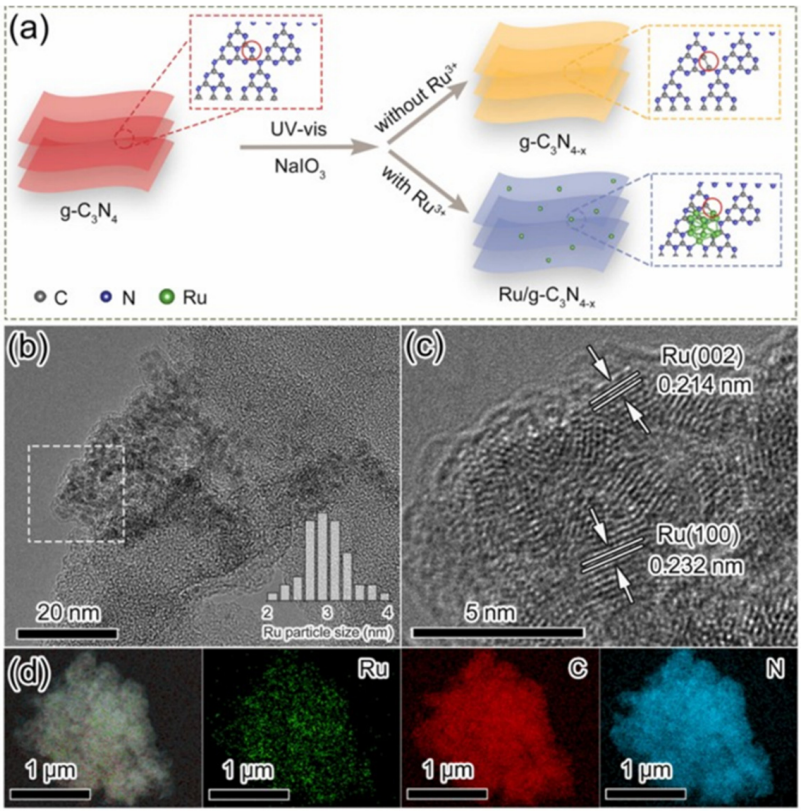

Figure 6. (**a**) Schematic illustration for the synthesis of g-C_3N_{4-x} and Ru/g-C_3N_{4-x}. (**b**) TEM image and Ru particle size distribution. (**c**) HRTEM image recorded on the area marked with a white rectangle in (**b**). (**d**) HAADF-STEM image and element mappings of Ru/g-C_3N_{4-x} photocatalyst.

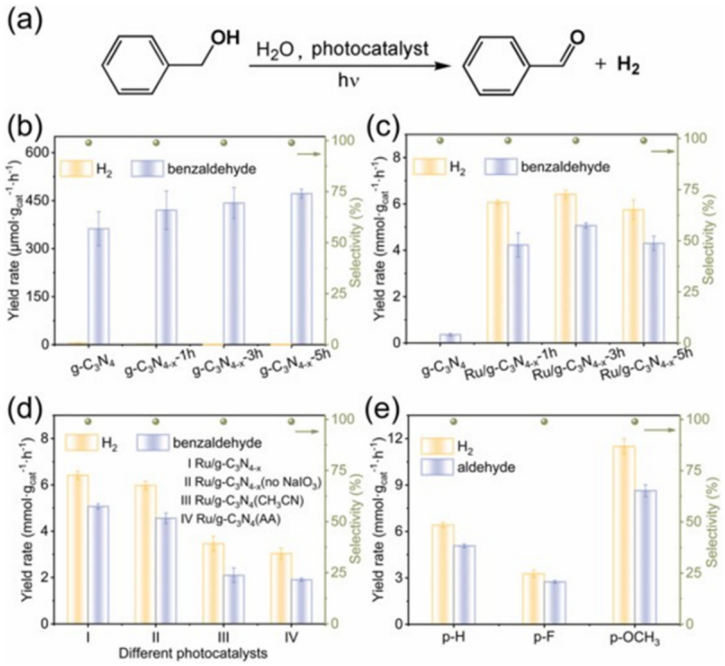

Figure 7. (**a**) Photocatalytic redox coupling reaction of H_2 evolution and benzyl alcohol oxidation. Production rates of H_2 and benzaldehyde over different photocatalysts or under different conditions: (**b**) $g\text{-}C_3N_{4-x}$ obtained at different irradiation durations. (**c**) $Ru/g\text{-}C_3N_{4-x}$ photocatalysts obtained at different irradiation durations. (**d**) Ru modified $g\text{-}C_3N_4$ photocatalysts prepared by different methods. (**e**) the optimal $Ru/g\text{-}C_3N_{4-x}$ photocatalyst in different substituted benzyl alcohol aqueous solutions.

2.2.3. Construction of Semiconductor/$g\text{-}C_3N_4$ Heterojunctions

The design and construction of semiconductor/$g\text{-}C_3N_4$ heterojunctions is regarded as an effective method to promote charge transfer and electron–hole pair separation. Among all kinds of $g\text{-}C_3N_4$ semiconductor heterojunctions reported in recent years, the $TiO_2/g\text{-}C_3N_4$ heterojunction demonstrates the most promising photocatalytic properties. Tan et al. developed a one-step synthesis method of nanostructured $g\text{-}C_3N_4/TiO_2$ heterojunctions (CN/TiO_2-24) [78]. The experimental data show that the efficiency of hydrogen evolution of $TiO_2/g\text{-}C_3N_4$ nano-heterojunctions is 10.8 times higher than that of $g\text{-}C_3N_4$ bulk under visible light irradiation, which is mainly attributed to the photoinduced electron–hole separation promoted by structure nanotization and heterojunction structure. As shown in Figure 8a,b, the XRD patterns and FT-IR spectra of the synthesized $TiO_2/g\text{-}C_3N_4$ and the control samples TiO_2 and $g\text{-}C_3N_4$ bulk are displayed, respectively. It can be seen that planarization of the $g\text{-}C_3N_4$ unit layer favors delocalization of π electrons, which will enhance the π-π superposition interaction and reduce the interlayer spacing. In other words, $g\text{-}C_3N_4$ with a larger surface area can produce more photogenerated charge carriers. Time courses of H_2 evolution on CN/TiO_2-24, nano-CN, $CN/TiO_{2\text{-mixture}}$, bulk-$CN/TiO_2$, bulk-CN, bulk-$CN/TiO_2$-mixture, and TiO_2 are shown in Figure 8c. The CN/TiO_2-24 heterojunction demonstrated the highest efficiency. The charge transfer path in the CN/TiO_2-24 heterojunction is shown in Figure 8d, which is a Type II heterostructure. The optically excited electrons in the $g\text{-}C_3N_4$ conduction band (CB) can be transferred to the TiO_2 CB to realize the efficient separation of photogenerated charge carriers. It can be seen that the nanotization of $g\text{-}C_3N_4$ and the heterostructure formed by the contact between $g\text{-}C_3N_4$ and TiO_2 synergistically inhibit the recombination of photogenerated carriers and improve the precipitation of hydrogen catalyzed by visible light of CN/TiO_2-24. In summary, the synergistic strategy of structural nanotization and heterojunction structure is a key factor to promote the efficient separation of photogenerated electron–hole pairs. This method and device can be used to fabricate other $g\text{-}C_3N_4$-based nanocomposites with advanced photocatalytic properties.

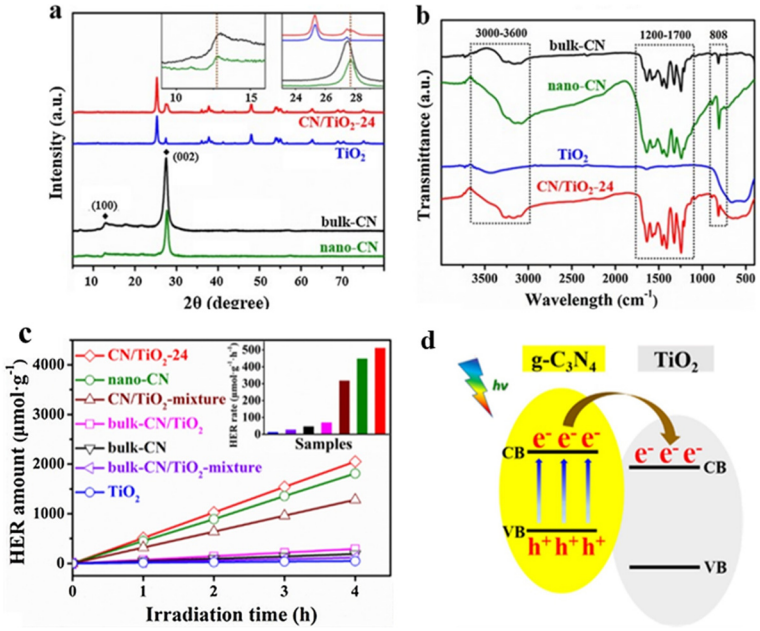

Figure 8. (**a**) XRD patterns and local magnifications (inserts) and (**b**) FT-IR spectra of CN/TiO_2-24, TiO_2, bulk-CN, and nano-CN. (**c**) Time courses of H_2 evolution on CN/TiO_2-24, nano-CN, $CN/TiO_{2\text{-mixture}}$, bulk-CN/$TiO_2$, bulk-CN, bulk-CN/$TiO_2$-mixture, and TiO_2; insert is the H_2 evolution rates. (**d**) Schematic diagram of electronic transfer mechanism.

2.2.4. Construction of Carbon/g-C_3N_4 Heterojunctions

Carbonaceous nanomaterials with π-conjugated structures, such as fullerenes, carbon nanotubes, graphene, carbon nanodots, etc., which usually have very unique structural and photoelectric properties, have been demonstrated to be effective carriers of nano-photocatalysts to delay the recombination of photogenerated electron–hole pairs. Chai et al. developed a fullerene-modified g-C_3N_4 (C_{60}/g-C_3N_4) heterojunction for efficient photocatalytic degradation of Rhodamine B [79]. Bai et al. developed the method of thermal polymerization of dicyandiamide together with C60 at 550 °C, and prepared a C_{60}/g-C_3N_4 nano-heterojunction [80]. It is worth noting that C60 is a closed-shell structure composed of 30 molecular orbitals and 60 π electrons, which is of great help in improving the electron transport efficiency. The SEM images of g-C_3N_4 and C_{60}/g-C_3N_4 samples are shown in Figure 9a,b, which demonstrated the formation of C_{60}/g-C_3N_4 heterojunction. The diffuse reflectance absorption spectra of C_{60}, g-C_3N_4 and C_{60}/g-C_3N_4 photocatalysts and the Mott–Schottky (MS) plots of the different catalysts film electrodes were displayed in Figure 9c,d. Due to the long exciton diffusion length of C60, the photogenerated electrons can migrate quickly and accumulate on the C60 nanoparticles, which in turn improves the charge separation rate of the effective redox reactions.

In recent years, 2D graphene materials with excellent carrier mobility, large surface area, high thermal conductivity, optical transparency, and good chemical stability have gradually attracted extensive attention in the field of photocatalysis. Xiang et al. synthesized metal-free graphene/g-C_3N_4 heterojunctions by a combined impregnation–chemical reduction approach followed by thermal calcination [81]. Graphene oxide (GO) was reduced to graphene using hydrazine hydrate as reducing agent, and the g-C_3N_4 was fixed on the surface of graphene by hybrid process to form a layered heterojunction structure, as shown in Figure 10a,b. As the graphene content increases, as shown in Figure 10c, the heterojunction exhibits stronger light absorption in the visible region, which is mainly attributed to the larger specific surface area. It can be concluded that the combination of graphene and g-C_3N_4 can provide more channels for electron conduction and inhibit the recombination process of electron–hole pairs, thus increasing the H_2 production.

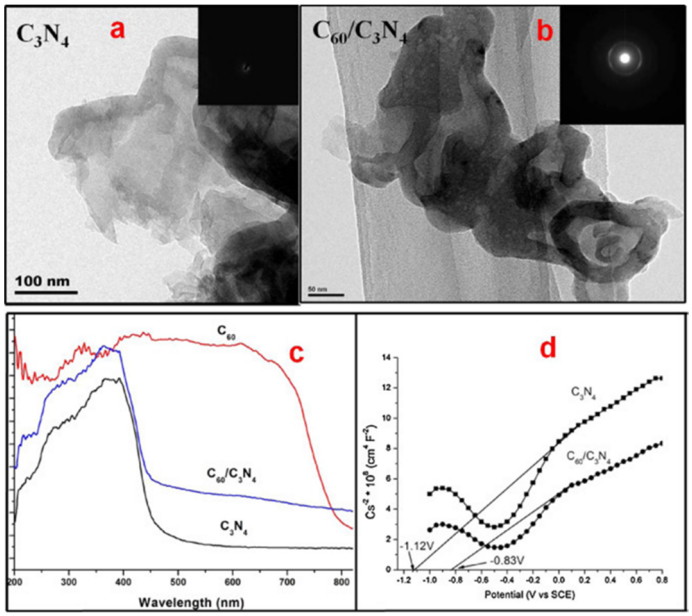

Figure 9. (**a**) TEM and SAED (insert) images of g-C_3N_4 photocatalyst. (**b**) TEM and SAED (insert) images of C_{60}/g-C_3N_4 photocatalyst. (**c**) Diffuse reflectance absorption spectra of C_{60}, g-C_3N_4, and C_{60}/g-C_3N_4 photocatalysts. (**d**) Mott–Schottky (MS) plots of the different catalysts film electrodes. The MS plots were obtained at a frequency of 1 kHz in an aqueous solution of Na_2SO_4 (0.1 M).

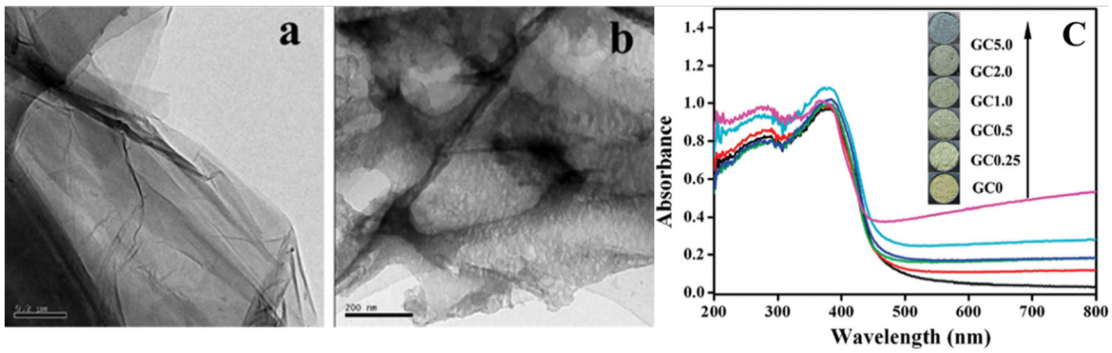

Figure 10. TEM images of graphene oxide (**a**,**b**) the GC1.0 sample. (**c**) UV−vis diffuse reflection spectra of the GC0, GC0.25, GC0.5, GC1.0, GC2.0, and GC5.0 samples. The inset shows their corresponding colors. Pure g-C_3N_4 (sample GC0) and graphene/g-C_3N_4 composites (samples GC0.25, GC0.5, GC1.0, GC2.0, and GC5.0).

Li et al. prepared a band-tunable rGO/g-C_3N_4 heterojunction by calcination of a mixture of cyanamide and GO in an Ar environment [82]. The experimental results show that the bandgap width of the rGO/g-C_3N_4 heterojunction decreases with the increase of graphene content, so as to realize the flexible regulation of the bandgap width. As shown in Figure 11a,b, when 10 vol% TEOA was introduced into the reaction system, the photocatalytic degradation efficiency significantly decreased. However, the photocatalytic degradation efficiency was almost not inhibited when the radical scavenger TBA was added to the reaction solution (h curve in Figure 11a). The above comparative experimental results show that the CN/rGO nanocomposite can realize the photocatalytic degradation of RhB by photohole oxidation under visible light irradiation. In addition, as shown in Figure 11c, the photocatalytic degradation efficiency only decreases by 1.1% after five repetitions, which indicates that the prepared CN/rGO photocatalyst has high repeatability and stability. In addition, the photocatalytic activities for the g-C_3N_4 and CN/rGO photocatalysis system towards 4-nitrophenol degradation for 150 min were displayed in Figure 11d. In short,

the above-mentioned literature provides new inroads into the development of metal-free graphene/g-C_3N_4 composite materials with a cornucopia of synthesis strategies for improved charge transfer and separation in the photocatalytic applications.

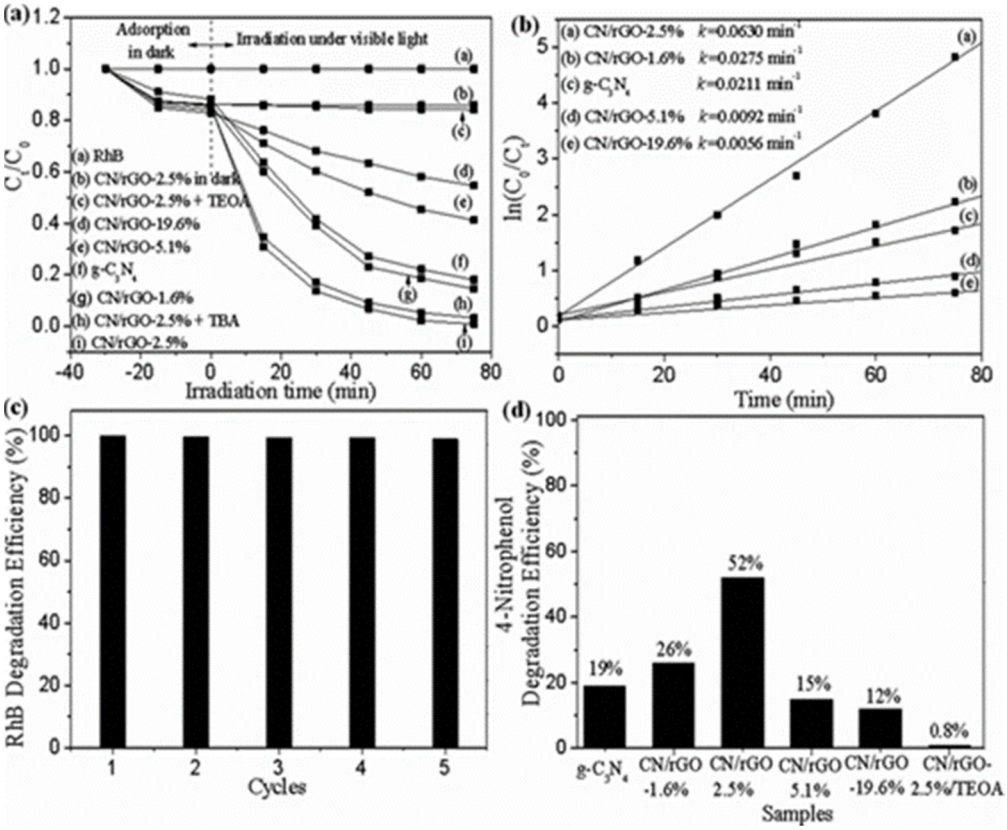

Figure 11. (**a**) Photocatalytic activities and (**b**) the degradation efficiency for the g-C_3N_4 and CN/rGO photocatalysis system. (**c**) Recycle test of CN/rGO-2.5% catalyst towards RhB degradation for 75 min and (**d**) photocatalytic activities for the g-C_3N_4 and CN/rGO photocatalysis system towards 4-nitrophenol degradation for 150 min.

2.2.5. Construction of Other g-C_3N_4-Based Heterojunctions

In this section, the heterojunction structure consisting of at least three elements is mainly discussed, and the modification of g-C_3N_4 with some selected complex compounds will be discussed below. For example, the Aurivillius-based semiconductor photocatalyst has drawn considerable attention as a promising candidate for the development of g-C_3N_4-based nanocomposites. The most-researched photocatalyst of Aurivillius-based material is Bi_2WO_6. Ge et al. prepared Bi_2WO_6/g-C_3N_4 heterostructured photocatalysts, which presented a strong absorption in the visible light region [83]. Figure 12a shows the XRD patterns of pure Bi_2WO_6 and g-C_3N_4, as well as of the g-C_3N_4/Bi_2WO_6 heterojunction, which demonstrated the formation of heterojunctions. As shown in Figure 12b,c, the transfer and separation efficiency of photogenerated carriers are significantly improved due to the synergistic interaction between g-C_3N_4 and Bi_2WO_6 and the binding of the electric field. When the photogenerated electrons of g-C_3N_4 are injected into the conduction band of Bi_2WO_6, the holes in the valence band of Bi_2WO_6 are transferred to the valence band of g-C_3N_4, which can delay the photogenerated carrier recombination and further improve the photocatalytic efficiency. Another work reported by Wang et al. also showed a successful fabrication of Bi_2WO_6/g-C_3N_4 photocatalysts for improvement of photocatalytic ability in methylene blue degradation.

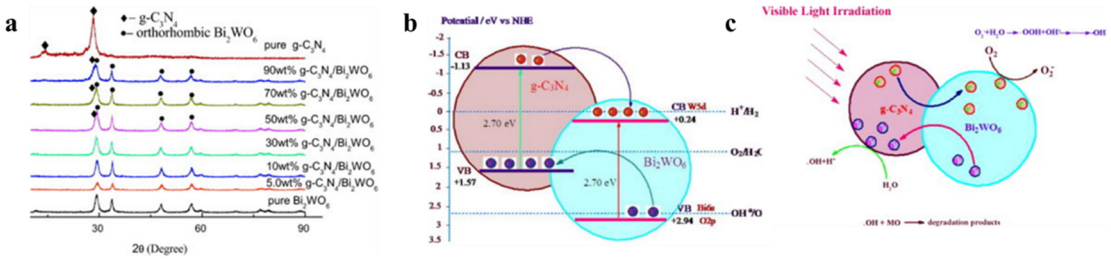

Figure 12. (**a**) XRD patterns of pure Bi_2WO_6 and g-C_3N_4, as well as of the g-C_3N_4/Bi_2WO_6 heterojunction photocatalysts. (**b**) Diagrams of the energy position and photogenerated electron–hole pair transfers between polymeric g-C_3N_4 and Bi_2WO_6. (**c**) Redox process of the g-C_3N_4/Bi_2WO_6 composite photocatalysts under visible light irradiation.

$BiVO_4$ has shown excellent chemical stability, visible light response, and high photocatalytic activity. Moreover, the three different crystals of $BiVO_4$ have different effects on the photocatalytic performance. For example, Li et al. fabricated a $BiVO_4$/g-C_3N_4 heterojunction by attaching discrete g-C_3N_4 nanoislands to a porous $BiVO_4$ [84]. As shown in Figure 13a,b, the diameters of the g-C_3N_4 are 5−10 nm. Moreover, it can be seen that g-C_3N_4 and $BiVO_4$ show good interface characteristics. The photocatalytic degradation experiments show that the as-synthesized g-C_3N_4/$BiVO_4$ heterojunction exhibited better visible photocatalytic activity for methyl blue, and its k value is 0.054/min, which is 4.5 times and 6.9 times that of pure $BiVO_4$ (0.012/min) and g-C_3N_4 (0.0078/min), respectively. This is mainly attributed to the higher charge separation efficiency of the heterojunction and the full exposure of the reaction site, thus enhancing the photocatalytic activity. The charge transfer mechanism is shown in Figure 13c. Furthermore, due to the disadvantages of a high recombination rate of photogenerated carriers and weak response to visible light of single $BiVO_4$, our group synthesized lanthanum-doped bismuth vanadate (La-$BiVO_4$) and oxygen-doped porous graphite carbon nitride (O-doped g-C_3N_4), i.e., La-$BiVO_4$/O-doped g-C_3N_4 powder by a facile hydrothermal reaction and low-temperature calcination, which will be discussed in detail in the next section.

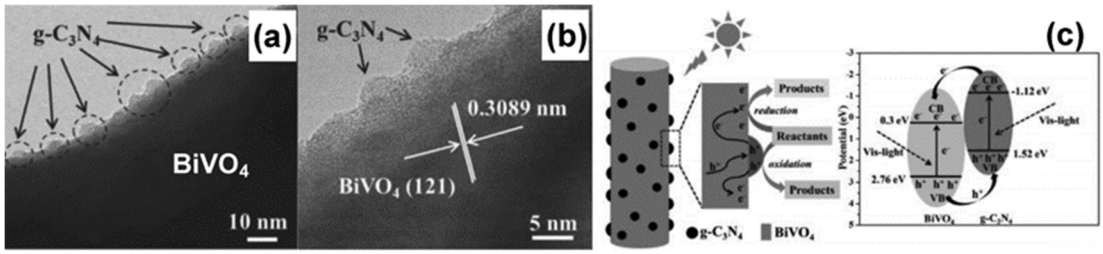

Figure 13. (**a**) TEM and (**b**) HRTEM images of monoclinic $BiVO_4$/g-C_3N_4 heterojunction photocatalysts. (**c**) Proposed schematic mechanism for charge transfer and separation in the $BiVO_4$/g-C_3N_4 sample under visible light irradiation.

In addition, the study shows that the heteroatom doping of g-C_3N_4 is also an effective way to increase the light absorption and improve the catalytic efficiency. Heteroatom doping produces shallow donor or acceptor levels. Furthermore, the band gap width and even the band structure are regulated. For example, Ye et al. added thiourea to melamine as a precursor, and then successfully deposited S-doped g-C_3N_4 films onto ITO substrates by the deposition process method of CVD [85]. Three heterojunctions with different structures were fabricated. Due to the doping of thiourea, the obtained S/g-C_3N_4 heterojunction exhibited a high and stable visible-light-driven photocurrent response.

3. Applications and Mechanism of g-C_3N_4-Based Heterojunction Photocatalytic Systems

In this section, practical applications and mechanisms of photocatalytic redox are summarized and discussed, such as water splitting for H_2 and O_2 evolution, reduction of CO_2 into hydrocarbon fuels, pollutant degradation and bacterial disinfection, etc.

3.1. Photocatalytic Water Splitting for H_2 and O_2 Generation

Energy shortages and the greenhouse effect have become the bottleneck problems of sustainable development of human society. The use of photocatalysts and solar energy to generate hydrogen from water is an ideal way to obtain new energy sources. At present, g-C_3N_4-based heterojunctions have been widely used in photocatalytic hydrogen production. The heterojunction structure design can promote the separation of photogenerated electron–hole pairs and effectively improve the photocatalytic efficiency [86–91].

Ji et al. synthesized a Cu_2O/g-C_3N_4 heterojunction via an in situ method [92]. As shown in Figure 14a, the XRD pattern of pure g-C_3N_4 has two distinct diffraction peaks at 13.1° and 27.4°, which are consistent with those reported in the literature. The nitrogen adsorption–desorption isotherms of the prepared samples are shown in Figure 14b. Both g-C_3N_4 and Cu_2O/g-C_3N_4 heterojunctions exhibit typical type IV isotherms with distinct hysteresis loops, indicating the presence of mesopores with pore sizes of 5–30 nm, as shown in Figure 14c. In addition, the FT-IR absorption peaks at 1327.3, 1417.1, 1581.1, and 1643.6 cm^{-1} belong to triangular C-N (-C)-C or bridge-C-N H-C units, as shown in Figure 14d. In addition, as shown in Figure 14e, the Cu_2O/g-C_3N_4 heterojunction (type II) showed stronger photocatalytic hydrogen production activity than the bulk g-C_3N_4. With the optimization of Cu_2O content, the visible photocatalytic hydrogen evolution rate can reach 33.2 μmol h^{-1} g^{-1}, which is about four times higher than that of pure g-C_3N_4. To investigate the photocatalytic stability of the Cu_2O/g-C_3N_4 heterojunction, a three-cycle hydrogen evolution experiment was carried out, as shown in Figure 14f. The results show that the three-cycle hydrogen evolution amount are almost the same, indicating that the hydrogen production stability of the Cu_2O/g-C_3N_4 heterojunction photocatalyst is good, which is mainly attributed to the improved separation and transfer efficiency of photogenerated electron–hole pairs by the Cu_2O/g-C_3N_4 heterojunction structure.

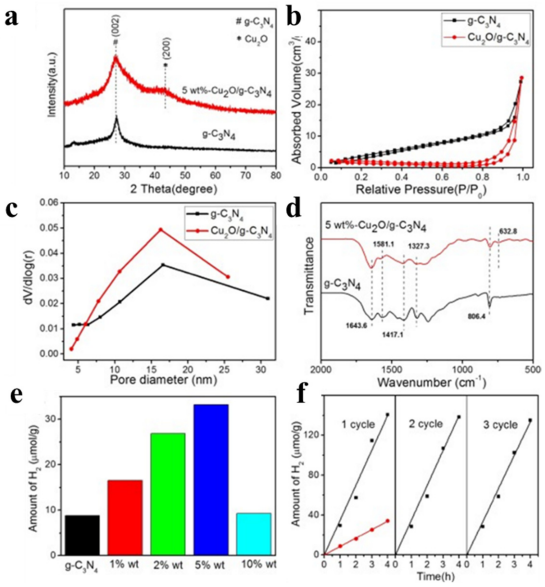

Figure 14. (**a**) XRD patterns. (**b**) Nitrogen absorption–desorption isotherms. (**c**) Pore diameter and (**d**) FT-IR spectra of pure g-C_3N_4 and 5 wt%-Cu_2O/g-C_3N_4. (**e**) Photocatalytic hydrogen evolution rates of bulk g-C_3N_4 and various Cu_2O/g-C_3N_4 samples under visible light (λ > 400 nm). (**f**) Time course of hydrogen evolution over 4 h for bulk g-C_3N_4 and 5 wt%-Cu_2O/g-C_3N_4 and cycling runs of 5 wt%-Cu_2O/g-C_3N_4 photocatalytic process under visible-light irradiation.

Wang et al. designed a 3D/2D straight Z-scheme g-C_3N_4-based heterojunction to facilitate charge separation for efficient solar hydrogen production [93]. The hydrothermal roasting method was adopted to prepare 3D TiO_2 microflowers/2D g-C_3N_4 nanosheets with Z-scheme heterostructures. As shown in Figure 15a, the optimal ratio of g-C_3N_4 in the heterojunction is 50% and its catalytic activity is 7.7 times and 1.9 times higher than that of pure g-C_3N_4 and TiO_2, respectively. The synergistic interaction between the highly dispersed 3D TiO_2 microflowers and 2D g-C_3N_4 nanosheets and the strong coupling caused by the efficient direct Z-scheme structure significantly improved the H_2 production activity, as shown in Figure 15b–d. The efficient separation of photogenerated carriers is demonstrated by the photoluminescence and photocurrent response results. These excellent photocatalytic properties further imply that the construction of 3D/2D Z-scheme heterojunctions is one of the effective ways to achieve high-speed solar H_2 production.

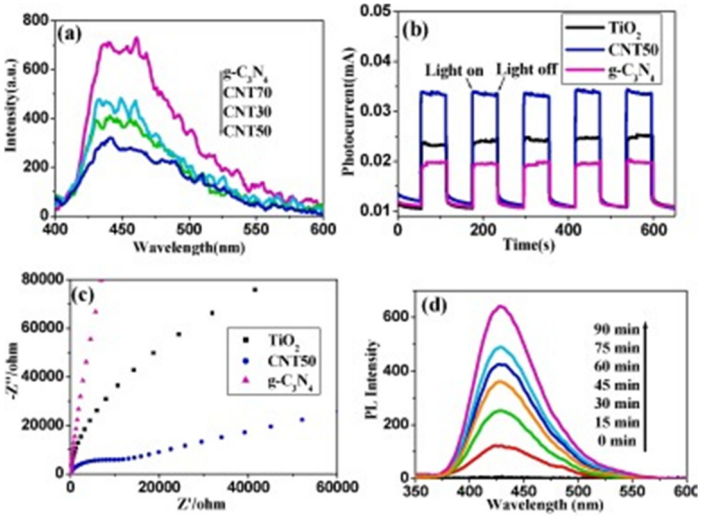

Figure 15. (**a**) PL spectra of g-C_3N_4, CNTx (x = 30, 50, and 70) photocatalysts under 320 nm excitation. (**b**) transient photocurrent responses of TiO_2, CNT50, g-C_3N_4 under illumination with a 300 W Xe lamp with a light intensity of 100 mW/cm^2. (**c**) Electrochemical impedance spectroscopy of TiO_2, CNT50, g-C_3N_4 and (**d**) PL spectral changes observed during irradiation of CNT50 sample in a 5×10^{-4} M basic solution of terephthalic acid (excitation at λ = 315 nm). Each fluorescence spectrum was recorded every 15 min interval.

3.2. Photocatalytic Reduction of CO_2 to Renewable Hydrocarbon Fuels

Recently, the increasingly serious greenhouse effect has posed a terrible threat to the survival of animals and plants on the earth. This is mainly due to carbon dioxide emissions from the burning of fossil fuels. Carbon neutrality is a strategic goal of China's economic and social development, and an important measure to promote the energy revolution and realize the progress of civilization. China aims to peak its carbon dioxide emissions by 2030 and achieve carbon neutrality by 2060. Therefore, how to improve the utilization of renewable energy and curb greenhouse gas emissions is of great significance. Studies show that photocatalytic reduction of CO_2 to renewable hydrocarbon fuels is one of the effective ways to solve the current dependence on fossil fuels and environmental pollution. However, due to the chemical stability and complex conversion processes, one-component catalysts usually do not satisfy all the prerequisites. The g-C_3N_4-based heterojunction has the advantages of wide light absorption and high charge transfer rate, which is an ideal material for photocatalytic reduction of CO_2 to renewable hydrocarbon fuels [27,94–96].

Cao et al. prepared In_2O_3/g-C_3N_4 heterojunctions (type II) by in situ growth of In_2O_3 nanocrystals on the surface of g-C_3N_4 sheet [97]. The XRD patterns and UV–vis absorption spectra of g-C_3N_4, In_2O_3, and 10 wt% In_2O_3/g-C_3N_4 are displayed in Figure 16a and 16b, respectively. The two diffraction peaks of g-C_3N_4 are 27.4° and 13.1°, which may be attributed to the (0 0 2) and (1 0 0) peaks of graphite material. It can be seen that the

In_2O_3/g-C_3N_4 heterojunction has the characteristic XRD peaks of both In_2O_3 and g-C_3N_4. In addition, photogenerated electrons and holes will be transferred at the interface between In_2O_3 and g-C_3N_4, which significantly improves the efficiency of charge separation and CO_2 reduction.

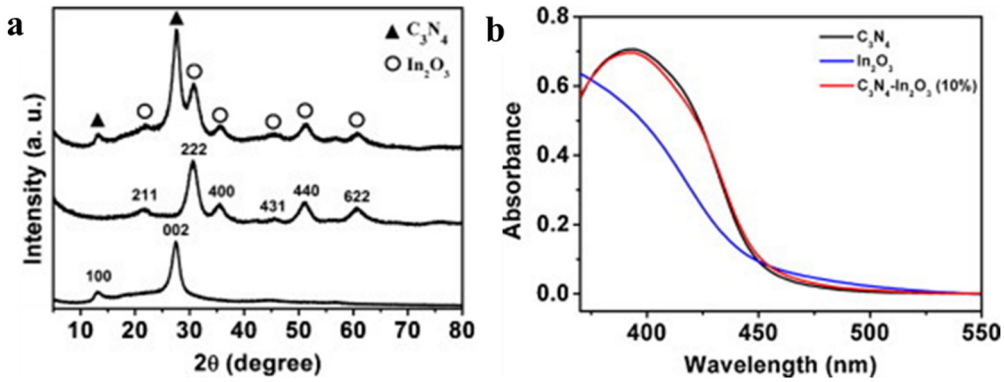

Figure 16. (**a**) XRD patterns of g-C_3N_4, In_2O_3, and 10 wt% In_2O_3/g-C_3N_4. (**b**) UV–vis absorption spectra of g-C_3N_4, In_2O_3, and 10 wt% In_2O_3/g-C_3N_4.

Li et al. synthesized a series of $LaPO_4$/g-C_3N_4 core–shell nanowire heterojunctions (type II) via an in situ hydrothermal growth of $LaPO_4$ nanorods in tubular g-C_3N_4 and investigated their photocatalytic activity in CO_2 reduction [98]. The g-C_3N_4 nanoshell wrapped on the $LaPO_4$ nanorod core is beneficial to improving the optical absorption efficiency and carrier separation/transfer ability. As shown in Figure 17a, the CO production of full-spectrum irradiated La/TCN-200 samples reached 0.433 μmol at the first hour, with an average of 14.43 μmol g^{-1} h^{-1}, which was 10.36 times and 8.07 times that of pure $LaPO_4$ and tCN, respectively. Figure 17b shows the stability of CO evolution on La/tCN-200 under continuous illumination for 24 h. No significant inactivation was observed throughout the test, indicating that the La/tCN-200 sample had good photostability. As shown in Figure 17c,d, a possible mechanism characterized by the activation of $LaPO_4$ that significantly facilitates the separation/transfer of photogenerated carriers was proposed. The above experiments indicate that this new La/tCN-200 heterojunction will be a promising material for reduction of CO_2 to renewable hydrocarbon fuels.

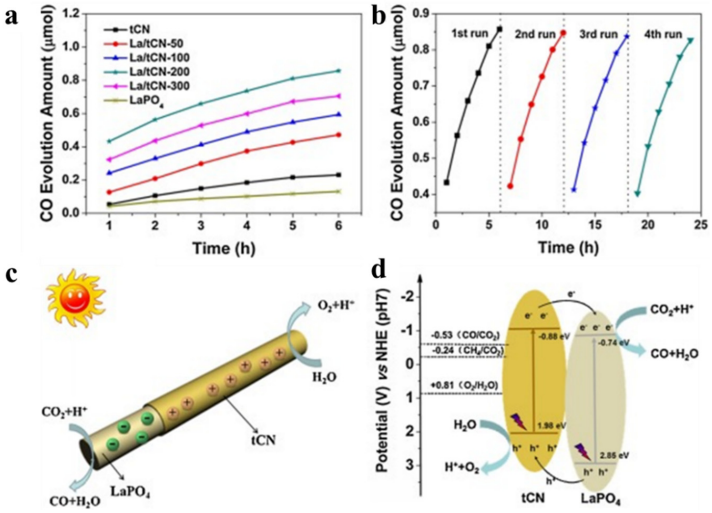

Figure 17. (**a**) Time-dependent CO_2 generation over tCN, $LaPO_4$, and La/tCN heterojunctions under full-spectrum irradiation. (**b**) Recycling stability tests over La/tCN-200. (**c**) Schematic illustration and (**d**) the proposed mechanism in the nano heterojunction.

3.3. Photocatalytic Degradation of Organic Pollutants

Photodegradation of organic pollutants is very important for the control of environmental pollution and has become a common concern of researchers [99–104]. In recent years, g-C_3N_4 or g-C_3N_4-based heterojunctions as ideal visible light active photocatalytic materials have been proven to have broad application prospects in various environmental aspects, such as photodegradation of various pollutants, air purification, water disinfection, and so on. Among them, organic pollutants such as rhodamine B (RhB), methylene blue (MB), methyl orange (MO), and phenol are widely used in the evaluation of photocatalytic performance [19,21,25,105–107].

Figure 18 shows the schematic diagram of the photocatalytic degradation of pollutants by g-C_3N_4. When g-C_3N_4 is irradiated by light, photogenerated electron–hole pairs are excited in g-C_3N_4. The photogenerated electrons react with the adsorbed molecule O_2 to generate $\bullet O^{2-}$ superoxide anion radicals, which in turn generate •OH radicals and H+, and ultimately lead to the degradation of organic pollutants.

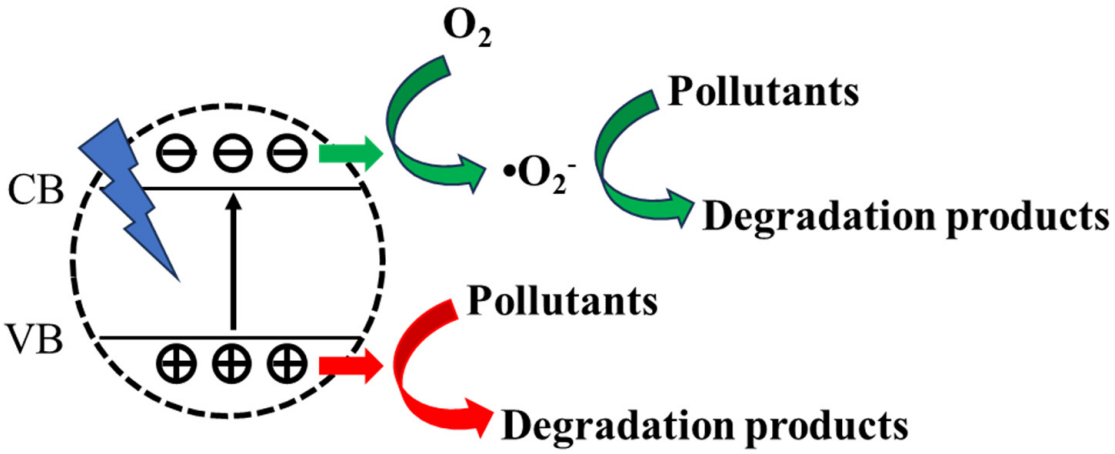

Figure 18. Schematic of photocatalytic degradation of pollutants under light irradiation using pristine g-C_3N_4 as a reference photocatalyst.

A method for the preparation of Z-scheme heterojunctions by hydrothermal loading Bi_2O_3 nanoparticles onto nitrogen vacant 2D g-C_3N_4 nanosheets was reported by Ghosh et al. [108]. The degradation process was mainly monitored by extraction of 1N acetic acid. The required time after illumination and the corresponding extraction concentration are shown in Figure 19a. The reaction kinetics of different samples are shown in Figure 19b. The experimental results show that the Bi_2O_3/g-C_3N_4 heterojunction exhibits good photocatalytic degradation effect under visible light irradiation. Among them, the 2% Bi_2O_3/g-C_3N_4 heterojunction obtains the highest degradation efficiency, with a first-order degradation rate constant of 0.040 min^{-1}, which is 2.5 times and 1.9 times higher than that of bulk and nitrogen vacant two-dimensional g-C_3N_4 nanosheets, respectively. In addition, based on the results of radical scavenging experiments, the electron transfer mechanism of the direct Z-scheme is proposed, as shown in Figure 19c,d. Jin et al. first successfully fabricated a series of efficient and stable Z-scheme $LaCoO_3$/g-C_3N_4 heterojunction photocatalysts with different weight contents of g-C_3N_4 by a facile one-step impregnation method [109]. The results show that Z-scheme heterostructures have formed on the interfaces between the perovskite-type oxides $LaCoO_3$ and the flake-like g-C_3N_4, which enhance the visible-light absorption, separation of the photogenerated electron–hole pairs, and transformation of the photogenerated electrons.

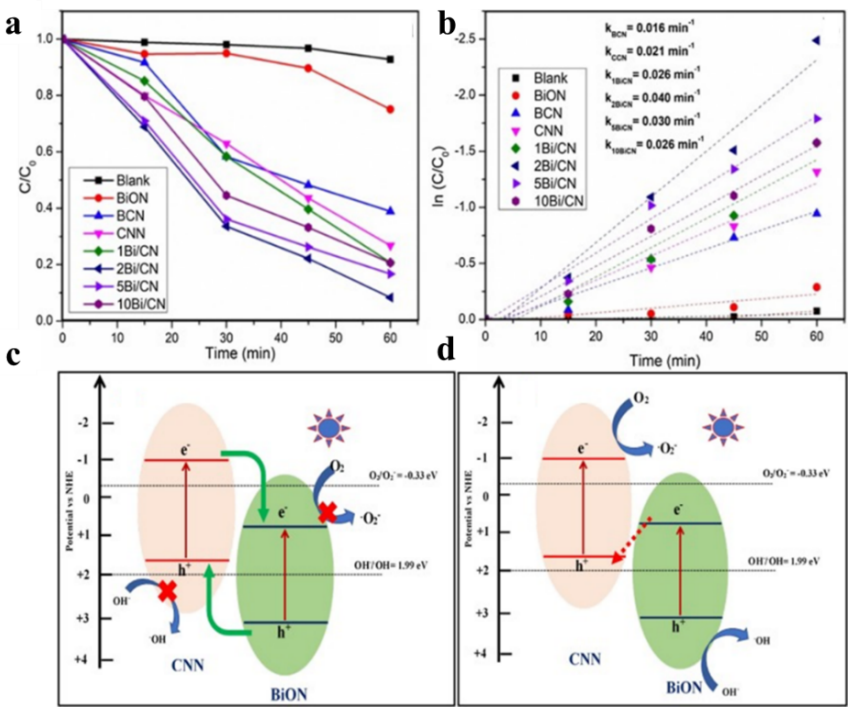

Figure 19. (**a**) Photocatalytic performance of BCN, CNN, and the Bi_2O_3/g-C_3N_4(Bi/CN) heterojunction. (**b**) plot of ln (C/C0) versus time. The two possible electron transfer mechanisms: (**c**) Type II heterostructure and (**d**) Z scheme mechanism.

Our group has made some progress in the photocatalytic degradation of aflatoxin and RhB by g-C_3N_4. As shown in Figure 20a–f, we fabricated three electrospun films composed of g-C_3N_4/MoS_2 heterojunctions [110]. Among the three samples, the highest photocatalytic degradation efficiency can reach 96.8%. In addition, a hybrid material consisting of La-$BiVO_4$ and O-doped g-C_3N_4 was prepared by a simple hydrothermal reaction and low-temperature calcination process [111]. The doping of La^{3+} ions and oxygen ions increased the specific surface area of the photocatalytic material. Moreover, the photocatalytic efficiency was further improved by constructing Z-scheme heterojunctions. We also delve into the mechanism of La^{3+} ion doping in promoting photogenerated carrier separation and broadening the optical absorption range. The experimental results show that the photocatalytic activity of the heterojunction material is about 2.85 times and two times higher than that of pure $BiVO_4$ and oxygen-doped g-C_3N_4, respectively. These results provide a method to study the preparation of high efficiency photocatalyst materials at low cost. The different types and applications of g-C_3N_4-based heterojunctions have been summarized in Table 1.

Table 1. Types and Applications of g-C_3N_4-Based Heterojunctions.

Photocatalysts	Type of Heterojunctions	Applications	References
TiO_2/g-C_3N_4	Type II	degradation of methyl orange (MO) and phenol	[112]
$Bi_2O_2CO_3$/g-C_3N_4	Type II	degradation of rhodamine B (RhB) and phenol	[113]
V_2O_5/g-C_3N_4	Z-scheme	degradation of RhB and tetracycline	[114]
Ag_3PO_4/g-C_3N_4	Z-scheme	degradation of sulfamethoxazole	[115]
MoS_2/g-C_3N_4	Type II	H_2 evolution	[116]
$CoTiO_3$/g-C_3N_4	Z-scheme	H_2 evolution	[117]
MnO_2/g-C_3N_4	Z-scheme	CO_2 reduction	[118]
red phosphor/g-C_3N_4	Type II	CO_2 reduction	[119]

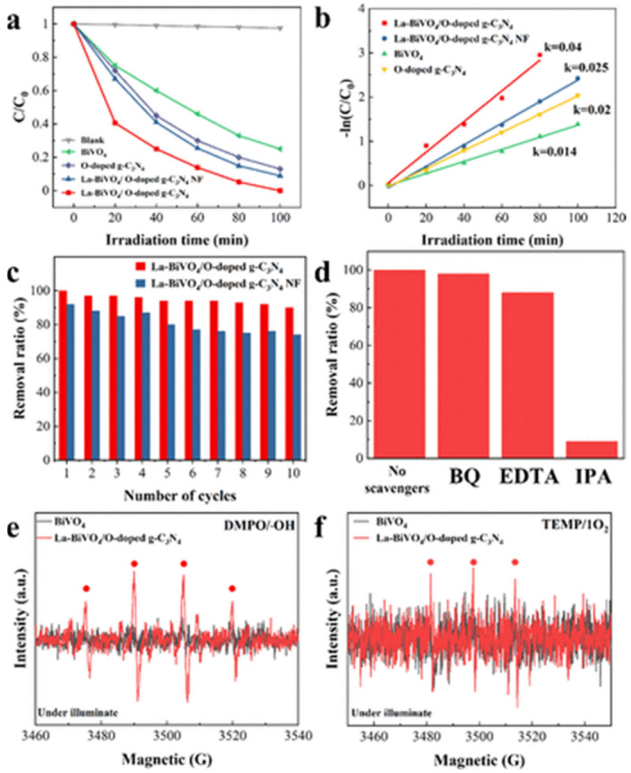

Figure 20. (**a**) Photocatalytic degradation of RhB over the obtained $BiVO_4$, O-doped g-C_3N_4, La-$BiVO_4$/O-doped g-C_3N_4 powder, and NF photocatalysts under simulated sunlight irradiation. (**b**) Corresponding kinetic plots. (**c**) Recyclability tests of La-$BiVO_4$/O-doped g-C_3N_4 powder and NFs for RhB degradation. (**d**) Photocatalytic degradation of RhB over La-$BiVO_4$/O-doped g-C_3N_4 for different scavengers, and (**e**,**f**) ESR spectra of (**e**) DMPO/•OH and (**f**) TEMP/$^1O_2$ in the presence of $BiVO_4$ and La-$BiVO_4$/O-doped g-C_3N_4.

4. Conclusions and Outlook

g-C_3N_4 is an ideal candidate for novel photocatalytic applications due to its low cost, high stability, and fast response to visible light. The synthesis of g-C_3N_4 materials was systematically reviewed and discussed. However, the fast recombination rate of g-C_3N_4-photogenerated carriers greatly diminishes its photocatalytic performance. Among the various methods to improve the photocatalytic efficiency, using two or more kinds of semiconductor materials to reasonably construct heterojunctions can comprehensively utilize the advantages of multiple components, improve the photogenerated carrier charge separation efficiency, increase the utilization rate of visible light, and maintain the high redox ability of electron–hole pairs. Therefore, in this review, we have divided the g-C_3N_4-based heterojunction photocatalysts into several major classes, namely, type II, Z-scheme, and type S heterojunction, which have been demonstrated to exhibit excellent photocatalytic efficiency in several photocatalytic applications.

However, according to the existing results, the photocatalytic efficiency and stability based on the g-C_3N_4 heterojunction still need to be improved. Especially compared with the current demand in photocatalytic industrial production, the gap is large. Therefore, some suggestions that can help to further improve the photocatalytic efficiency are summarized.

1. More stable and efficient heterojunction structure designs need to be developed for superior redox efficiency.
2. New strategies must be exploited to increase the light-harvesting ability of g-C_3N_4-based heterojunctions to utilize higher wavelengths of light (500 nm or near-infrared) to imitate natural photosynthesis in plants.

3. Multifield applications must be integrated into one photocatalytic system; this is an ideal catalytic procedure which may require the hybridization of multifunctional materials with reasonable energy structures to construct the g-C_3N_4-based heterojunction.
4. More theoretical studies about g-C_3N_4-based heterojunction need to be combined with practical catalytic applications. It is certain the in-depth fundamental theory based on physical chemistry research collaborated with laboratory findings will positively promote the advances in materials science and technology.

Finally, it is hoped that this review will provide future researchers with a better understanding of g-C_3N_4-based heterojunction synthesis and engineering methods, and guide further development of more efficient g-C_3N_4-based heterojunction photocatalyst. It is settled that g-C_3N_4-based heterojunction can shine brilliantly in the photocatalysis field and extraordinarily contribute to addressing the global energy and environmental crisis in the approaching days.

Author Contributions: The manuscript was written through contributions of all authors. All authors have read and agreed to the published version of the manuscript.

Funding: This work was supported by the Shanghai Post-doctoral Excellence Program (Grant No. 2022476).

Data Availability Statement: No new data were created or analyzed in this study.

Conflicts of Interest: The authors report no conflicts of interest.

References

1. Weng, B.; Qi, M.-Y.; Han, C.; Tang, Z.-R.; Xu, Y.-J. Photocorrosion Inhibition of Semiconductor-Based Photocatalysts: Basic Principle, Current Development, and Future Perspective. *ACS Catal.* **2019**, *9*, 4642–4687. [CrossRef]
2. Meng, X.; Liu, L.; Ouyang, S.; Xu, H.; Wang, D.; Zhao, N.; Ye, J. Nanometals for Solar-to-Chemical Energy Conversion: From Semiconductor-Based Photocatalysis to Plasmon-Mediated Photocatalysis and Photo-Thermocatalysis. *Adv. Mater.* **2016**, *28*, 6781–6803. [CrossRef] [PubMed]
3. Chen, F.; Huang, H.; Guo, L.; Zhang, Y.; Ma, T. The Role of Polarization in Photocatalysis. *Angew. Chem. Int. Ed.* **2019**, *58*, 10061–10073. [CrossRef] [PubMed]
4. Hu, C.; Tu, S.; Tian, N.; Ma, T.; Zhang, Y.; Huang, H. Photocatalysis Enhanced by External Fields. *Angew. Chem. Int. Ed.* **2021**, *60*, 16309–16328. [CrossRef]
5. Kisch, H. Semiconductor PhotocatalysisMechanistic and Synthetic Aspects. *Angew. Chem.-Int. Ed.* **2013**, *52*, 812–847. [CrossRef]
6. Ibhadon, A.O.; Fitzpatrick, P. Heterogeneous Photocatalysis: Recent Advances and Applications. *Catalysts* **2013**, *3*, 189–218. [CrossRef]
7. Wang, M.; Ioccozia, J.; Sun, L.; Lin, C.; Lin, Z. Inorganic-modified semiconductor TiO_2 nanotube arrays for photocatalysis. *Energy Environ. Sci.* **2014**, *7*, 2182–2202. [CrossRef]
8. Huang, H.; Pradhan, B.; Hofkens, J.; Roeffaers, M.B.J.; Steele, J.A. Solar-Driven Metal Halide Perovskite Photocatalysis: Design, Stability, and Performance. *ACS Energy Lett.* **2020**, *5*, 1107–1123. [CrossRef]
9. Wen, J.; Li, X.; Liu, W.; Fang, Y.; Xie, J.; Xu, Y. Photocatalysis fundamentals and surface modification of TiO_2 nanomaterials. *Chin. J. Catal.* **2015**, *36*, 2049–2070. [CrossRef]
10. Li, B.; Lai, C.; Zeng, G.; Huang, D.; Qin, L.; Zhang, M.; Cheng, M.; Liu, X.; Yi, H.; Zhou, C.; et al. Black Phosphorus, a Rising Star 2D Nanomaterial in the Post-Graphene Era: Synthesis, Properties, Modifications, and Photocatalysis Applications. *Small* **2019**, *15*, e1804565. [CrossRef]
11. Tang, C.; Cheng, M.; Lai, C.; Li, L.; Yang, X.; Du, L.; Zhang, G.; Wang, G.; Yang, L. Recent progress in the applications of non-metal modified graphitic carbon nitride in photocatalysis. *Coord. Chem. Rev.* **2023**, *474*, 214846. [CrossRef]
12. Wang, J.; Wang, S. A critical review on graphitic carbon nitride (g-C_3N_4)-based materials: Preparation, modification and environmental application. *Coord. Chem. Rev.* **2022**, *453*, 214338. [CrossRef]
13. Alaghmandfard, A.; Ghandi, K. A Comprehensive Review of Graphitic Carbon Nitride (g-C_3N_4)-Metal Oxide-Based Nanocomposites: Potential for Photocatalysis and Sensing. *Nanomaterials* **2022**, *12*, 294. [CrossRef] [PubMed]
14. Fu, J.; Yu, J.; Jiang, C.; Cheng, B. g-C_3N_4-Based Heterostructured Photocatalysts. *Adv. Energy Mater.* **2018**, *8*, 1701503. [CrossRef]
15. Cao, S.; Low, J.; Yu, J.; Jaroniec, M. Polymeric Photocatalysts Based on Graphitic Carbon Nitride. *Adv. Mater.* **2015**, *27*, 2150–2176. [CrossRef]
16. Prasad, C.; Tang, H.; Liu, Q.; Bahadur, I.; Karlapudi, S.; Jiang, Y. A latest overview on photocatalytic application of g-C_3N_4 based nanostructured materials for hydrogen production. *Int. J. Hydrogen Energy* **2020**, *45*, 337–379. [CrossRef]
17. Huang, Y.; Mei, F.; Zhang, J.; Dai, K.; Dawson, G. Construction of 1D/2D $W_{18}O_{49}$/Porous g-C_3N_4 S-Scheme Heterojunction with Enhanced Photocatalytic H-2 Evolution. *Acta Phys. Chim. Sin.* **2022**, *38*, 2108028. [CrossRef]

18. Sun, T.; Li, C.; Bao, Y.; Fan, J.; Liu, E. S-Scheme $MnCo_2S_4$/g-C_3N_4 Heterojunction Photocatalyst for H_2 Production. *Acta Phys. Chim. Sin.* **2023**, *39*, 2212009. [CrossRef]
19. Zhou, L.; Li, Y.; Zhang, Y.; Qiu, L.; Xing, Y. A 0D/2D $Bi_4V_2O_{11}$/g-C_3N_4 S-Scheme Heterojunction with Rapid Interfacial Charges Migration for Photocatalytic Antibiotic Degradation. *Acta Phys. Chim. Sin.* **2022**, *38*, 2112027. [CrossRef]
20. Xu, M.-L.; Lu, M.; Qin, G.-Y.; Wu, X.-M.; Yu, T.; Zhang, L.-N.; Li, K.; Cheng, X.; Lan, Y.-Q. Piezo-Photocatalytic Synergy in $BiFeO_3$@COF Z-Scheme Heterostructures for High-Efficiency Overall Water Splitting. *Angew. Chem. Int. Ed.* **2022**, *61*, e202210700. [CrossRef]
21. Duan, P.; Pan, J.; Du, W.; Yue, Q.; Gao, B.; Xu, X. Activation of peroxymonosulfate via mediated electron transfer mechanism on single-atom Fe catalyst for effective organic pollutants removal. *Appl. Catal. B Environ.* **2021**, *299*, 120714. [CrossRef]
22. Bai, J.; Shen, R.; Jiang, Z.; Zhang, P.; Li, Y.; Li, X. Integration of 2D layered CdS/WO_3 S-scheme heterojunctions and metallic Ti_3C_2 MXene-based Ohmic junctions for effective photocatalytic H-2 generation. *Chin. J. Catal.* **2022**, *43*, 359–369. [CrossRef]
23. Chen, T.; Yu, K.; Dong, C.; Yuan, X.; Gong, X.; Lian, J.; Cao, X.; Li, M.; Zhou, L.; Hu, B.; et al. Advanced photocatalysts for uranium extraction: Elaborate design and future perspectives. *Coord. Chem. Rev.* **2022**, *467*, 214615. [CrossRef]
24. Xue, Z.-H.; Luan, D.; Zhang, H.; Lou, X.W. Single-atom catalysts for photocatalytic energy conversion. *Joule* **2022**, *6*, 92–133. [CrossRef]
25. Sun, P.; Liu, Y.; Mo, F.; Wu, M.; Xiao, Y.; Xiao, X.; Wang, W.; Dong, X. Efficient photocatalytic degradation of high-concentration moxifloxacin over dodecyl benzene sulfonate modified graphitic carbon nitride: Enhanced photogenerated charge separation and pollutant enrichment. *J. Clean. Prod.* **2023**, *393*, 136320. [CrossRef]
26. Shi, W.; Sun, W.; Liu, Y.; Zhang, K.; Sun, H.; Lin, X.; Hong, Y.; Guo, F. A self-sufficient photo-Fenton system with coupling in-situ production H_2O_2 of ultrathin porous g-C_3N_4 nanosheets and amorphous FeOOH quantum dots. *J. Hazard. Mater.* **2022**, *436*, 129141. [CrossRef]
27. Li, H.; Yu, J.; Gong, Y.; Lin, N.; Yang, Q.; Zhang, X.; Wang, Y. Perovskite catalysts with different dimensionalities for environmental and energy applications: A review. *Sep. Purif. Technol.* **2023**, *307*, 122716. [CrossRef]
28. Chen, Y.; Cheng, M.; Lai, C.; Wei, Z.; Zhang, G.; Li, L.; Tang, C.; Du, L.; Wang, G.; Liu, H. The Collision between g-C_3N_4 and QDs in the Fields of Energy and Environment: Synergistic Effects for Efficient Photocatalysis. *Small* **2023**, *19*, e2205902. [CrossRef] [PubMed]
29. Demirci, S.; Sahiner, N. Use of Heteroatom-Doped g-C_3N_4 Particles as Catalysts for Dehydrogenation of Sodium Borohydride in Methanol. *C J. Carbon Res.* **2022**, *8*, 53. [CrossRef]
30. Huang, D.; Yan, X.; Yan, M.; Zeng, G.; Zhou, C.; Wan, J.; Cheng, M.; Xue, W. Graphitic Carbon Nitride-Based Heterojunction Photoactive Nanocomposites: Applications and Mechanism Insight. *ACS Appl. Mater. Interfaces* **2018**, *10*, 21035–21055. [CrossRef]
31. Wang, Y.; Zhang, M.; Wang, L.; Xing, J. Graphitic Carbon Nitride Emitter: From Structural Modification to Optoelectronics Applications. *Adv. Opt. Mater.* **2023**, *11*, 2301547. [CrossRef]
32. Fernandez-Catala, J.; Greco, R.; Navlani-Garcia, M.; Cao, W.; Berenguer-Murcia, A.; Cazorla-Amoros, D. g-C_3N_4-Based Direct Z-Scheme Photocatalysts for Environmental Applications. *Catalysts* **2022**, *12*, 1137. [CrossRef]
33. Kumar, S.; Karthikeyan, S.; Lee, A.F. g-C_3N_4-Based Nanomaterials for Visible Light-Driven Photocatalysis. *Catalysts* **2018**, *8*, 74. [CrossRef]
34. Wang, Y.; Zhong, S.; Niu, Z.; Dai, Y.; Li, J. Synthesis and up-to-date applications of 2D microporous g-C_3N_4 nanomaterials for sustainable development. *Chem. Commun.* **2023**, *59*, 10883–10911. [CrossRef] [PubMed]
35. Liao, G.; Gong, Y.; Zhang, L.; Gao, H.; Yang, G.-J.; Fang, B. Semiconductor polymeric graphitic carbon nitride photocatalysts: The "holy grail" for the photocatalytic hydrogen evolution reaction under visible light. *Energy Environ. Sci.* **2019**, *12*, 2080–2147. [CrossRef]
36. Safaei, J.; Mohamed, N.A.; Noh, M.F.M.; Soh, M.F.; Ludin, N.A.; Ibrahim, M.A.; Isahak, W.N.R.W.; Teridi, M.A.M. Graphitic carbon nitride (g-C_3N_4) electrodes for energy conversion and storage: A review on photoelectrochemical water splitting, solar cells and supercapacitors. *J. Mater. Chem. A* **2018**, *6*, 22346–22380. [CrossRef]
37. Xu, X.; Xu, Y.; Liang, Y.; Long, H.; Chen, D.; Hu, H.; Ou, J.Z. Vacancy-modified g-C_3N_4 and its photocatalytic applications. *Mater. Chem. Front.* **2022**, *6*, 3143–3173. [CrossRef]
38. Solayman, H.M.; Abd Aziz, A.; Yahya, N.Y.; Leong, K.H.; Sim, L.C.; Hossain, M.K.; Khan, M.B.; Zoh, K.-D. CQDs embed g-C_3N_4 photocatalyst in dye removal and hydrogen evolution: An insight review. *J. Water Process Eng.* **2024**, *57*, 104645. [CrossRef]
39. Shuaibu, A.S.; Hafeez, H.Y.; Mohammed, J.; Dankawu, U.M.; Ndikilar, C.E.; Suleiman, A.B. Progress on g-C_3N_4 based heterojunction photocatalyst for H_2 production via Photocatalytic water splitting. *J. Alloys Compd.* **2024**, *1002*, 175062. [CrossRef]
40. Jourshabani, M.; Lee, B.-K.; Shariatinia, Z. From Traditional Strategies to Z-scheme Configuration in Graphitic Carbon Nitride Photocatalysts: Recent Progress and Future Challenges. *Appl. Catal. B Environ.* **2020**, *276*, 119157. [CrossRef]
41. Zhao, Y.; Zhang, J.; Qu, L. Graphitic Carbon Nitride/Graphene Hybrids as New Active Materials for Energy Conversion and Storage. *Chemnanomat* **2015**, *1*, 298–318. [CrossRef]
42. Zheng, Y.; Lin, L.; Wang, B.; Wang, X. Graphitic Carbon Nitride Polymers toward Sustainable Photoredox Catalysis. *Angew. Chem. Int. Ed.* **2015**, *54*, 12868–12884. [CrossRef]
43. Nasir, M.S.; Yang, G.; Ayub, I.; Wang, S.; Wang, L.; Wang, X.; Yan, W.; Peng, S.; Ramakarishna, S. Recent development in graphitic carbon nitride based photocatalysis for hydrogen generation. *Appl. Catal. B Environ.* **2019**, *257*, 117855. [CrossRef]

44. Ding, M.; Zhou, J.; Yang, H.; Cao, R.; Zhang, S.; Shao, M.; Xu, X. Synthesis of Z-scheme g-C_3N_4 nanosheets/Ag_3PO_4 photocatalysts with enhanced visible-light photocatalytic performance for the degradation of tetracycline and dye. *Chin. Chem. Lett.* **2020**, *31*, 71–76. [CrossRef]
45. Wang, Y.; Yang, W.; Chen, X.; Wang, J.; Zhu, Y. Photocatalytic activity enhancement of core-shell structure g-C_3N_4@TiO_2 via controlled ultrathin g-C_3N_4 layer. *Appl. Catal. B Environ.* **2018**, *220*, 337–347. [CrossRef]
46. Sudhaik, A.; Raizada, P.; Shandilya, P.; Jeong, D.-Y.; Lim, J.-H.; Singh, P. Review on fabrication of graphitic carbon nitride based efficient nanocomposites for photodegradation of aqueous phase organic pollutants. *J. Ind. Eng. Chem.* **2018**, *67*, 28–51. [CrossRef]
47. Goettmann, F.; Fischer, A.; Antonietti, M.; Thomas, A. Metal-free catalysis of sustainable Friedel-Crafts reactions: Direct activation of benzene by carbon nitrides to avoid the use of metal chlorides and halogenated compounds. *Chem. Commun.* **2006**, *43*, 4530–4532. [CrossRef]
48. Ong, W.-J.; Tan, L.-L.; Ng, Y.H.; Yong, S.-T.; Chai, S.-P. Graphitic Carbon Nitride (g-C_3N_4)-Based Photocatalysts for Artificial Photosynthesis and Environmental Remediation: Are We a Step Closer to Achieving Sustainability? *Chem. Rev.* **2016**, *116*, 7159–7329. [CrossRef]
49. Iqbal, W.; Yang, B.; Zhao, X.; Rauf, M.; Waqas, M.; Gong, Y.; Zhang, J.; Mao, Y. Controllable synthesis of graphitic carbon nitride nanomaterials for solar energy conversion and environmental remediation: The road travelled and the way forward. *Catal. Sci. Technol.* **2018**, *8*, 4576–4599. [CrossRef]
50. Niu, P.; Zhang, L.; Liu, G.; Cheng, H.-M. Graphene-Like Carbon Nitride Nanosheets for Improved Photocatalytic Activities. *Adv. Funct. Mater.* **2012**, *22*, 4763–4770. [CrossRef]
51. She, X.; Xu, H.; Xu, Y.; Yan, J.; Xia, J.; Xu, L.; Song, Y.; Jiang, Y.; Zhang, Q.; Li, H. Exfoliated graphene-like carbon nitride in organic solvents: Enhanced photocatalytic activity and highly selective and sensitive sensor for the detection of trace amounts of Cu^{2+}. *J. Mater. Chem. A* **2014**, *2*, 2563–2570. [CrossRef]
52. Yin, Y.; Han, J.; Zhang, X.; Zhang, Y.; Zhou, J.; Muir, D.; Sutarto, R.; Zhang, Z.; Liu, S.; Song, B. Facile synthesis of few-layer-thick carbon nitride nanosheets by liquid ammonia-assisted lithiation method and their photocatalytic redox properties. *RSC Adv.* **2014**, *4*, 32690–32697. [CrossRef]
53. Tong, J.; Zhang, L.; Li, F.; Wang, K.; Han, L.; Cao, S. Rapid and high-yield production of g-C_3N_4 nanosheets via chemical exfoliation for photocatalytic H-2 evolution. *RSC Adv.* **2015**, *5*, 88149–88153. [CrossRef]
54. Li, M.; Zhang, L.; Fan, X.; Zhou, Y.; Wu, M.; Shi, J. Highly selective CO_2 photoreduction to CO over g-C_3N_4/Bi_2WO_6 composites under visible light. *J. Mater. Chem. A* **2015**, *3*, 5189–5196. [CrossRef]
55. Zhang, X.; Xie, X.; Wang, H.; Zhang, J.; Pan, B.; Xie, Y. Enhanced Photoresponsive Ultrathin Graphitic-Phase C_3N_4 Nanosheets for Bioimaging. *J. Am. Chem. Soc.* **2013**, *135*, 18–21. [CrossRef]
56. Pawar, R.C.; Kang, S.; Park, J.H.; Kim, J.-H.; Ahn, S.; Lee, C.S. Room-temperature synthesis of nanoporous 1D microrods of graphitic carbon nitride (g-C_3N_4) with highly enhanced photocatalytic activity and stability. *Sci. Rep.* **2016**, *6*, 31147. [CrossRef]
57. Han, Q.; Wang, B.; Zhao, Y.; Hu, C.; Qu, L. A Graphitic-C_3N_4 "Seaweed" Architecture for Enhanced Hydrogen Evolution. *Angew. Chem. Int. Ed.* **2015**, *54*, 11433–11437. [CrossRef]
58. Zheng, Y.; Lin, L.; Ye, X.; Guo, F.; Wang, X. Helical Graphitic Carbon Nitrides with Photocatalytic and Optical Activities. *Angew. Chem. Int. Ed.* **2014**, *53*, 11926–11930. [CrossRef]
59. Li, X.-H.; Zhang, J.; Chen, X.; Fischer, A.; Thomas, A.; Antonietti, M.; Wang, X. Condensed Graphitic Carbon Nitride Nanorods by Nanoconfinement: Promotion of Crystallinity on Photocatalytic Conversion. *Chem. Mater.* **2011**, *23*, 4344–4348. [CrossRef]
60. Zhang, J.; Guo, F.; Wang, X. An Optimized and General Synthetic Strategy for Fabrication of Polymeric Carbon Nitride Nanoarchitectures. *Adv. Funct. Mater.* **2013**, *23*, 3008–3014. [CrossRef]
61. Shi, Y.; Wan, Y.; Zhao, D. Ordered mesoporous non-oxide materials. *Chem. Soc. Rev.* **2011**, *40*, 3854–3878. [CrossRef] [PubMed]
62. Wang, S.; Li, C.; Wang, T.; Zhang, P.; Li, A.; Gong, J. Controllable synthesis of nanotube-type graphitic C_3N_4 and their visible-light photocatalytic and fluorescent properties. *J. Mater. Chem. A* **2014**, *2*, 2885–2890. [CrossRef]
63. Liang, C.; Li, Z.; Dai, S. Mesoporous carbon materials: Synthesis and modification. *Angew. Chem. Int. Ed.* **2008**, *47*, 3696–3717. [CrossRef] [PubMed]
64. Zhang, Y.; Liu, J.; Wu, G.; Chen, W. Porous graphitic carbon nitride synthesized via direct polymerization of urea for efficient sunlight-driven photocatalytic hydrogen production. *Nanoscale* **2012**, *4*, 5300–5303. [CrossRef]
65. Wang, Y.; Wang, X.; Antonietti, M.; Zhang, Y. Facile One-Pot Synthesis of Nanoporous Carbon Nitride Solids by Using Soft Templates. *Chemsuschem* **2010**, *3*, 435–439. [CrossRef]
66. Goettmann, F.; Fischer, A.; Antonietti, M.; Thomas, A. Chemical synthesis of mesoporous carbon nitrides using hard templates and their use as a metal-free catalyst for friedel-crafts reaction of benzene. *Angew. Chem. Int. Ed.* **2006**, *45*, 4467–4471. [CrossRef]
67. Wang, J.; Zhang, C.; Shen, Y.; Zhou, Z.; Yu, J.; Li, Y.; Wei, W.; Liu, S.; Zhang, Y. Environment-friendly preparation of porous graphite-phase polymeric carbon nitride using calcium carbonate as templates, and enhanced photoelectrochemical activity. *J. Mater. Chem. A* **2015**, *3*, 5126–5131. [CrossRef]
68. Kamat, P.V. Manipulation of Charge Transfer Across Semiconductor Interface. A Criterion That Cannot Be Ignored in Photocatalyst Design. *J. Phys. Chem. Lett.* **2012**, *3*, 663–672. [CrossRef] [PubMed]
69. Perera, S.D.; Mariano, R.G.; Khiem, V.; Nour, N.; Seitz, O.; Chabal, Y.; Balkus, K.J., Jr. Hydrothermal Synthesis of Graphene-TiO_2 Nanotube Composites with Enhanced Photocatalytic Activity. *ACS Catal.* **2012**, *2*, 949–956. [CrossRef]

70. Woan, K.; Pyrgiotakis, G.; Sigmund, W. Photocatalytic Carbon-Nanotube-TiO_2 Composites. *Adv. Mater.* **2009**, *21*, 2233–2239. [CrossRef]
71. Zhou, K.; Zhu, Y.; Yang, X.; Jiang, X.; Li, C. Preparation of graphene-TiO_2 composites with enhanced photocatalytic activity. *New J. Chem.* **2011**, *35*, 353–359. [CrossRef]
72. Furube, A.; Asahi, T.; Masuhara, H.; Yamashita, H.; Anpo, M. Charge carrier dynamics of standard TiO_2 catalysts revealed by femtosecond diffuse reflectance spectroscopy. *J. Phys. Chem. B* **1999**, *103*, 3120–3127. [CrossRef]
73. Liu, B.; Aydil, E.S. Anatase TiO_2 films with reactive {001} facets on transparent conductive substrate. *Chem. Commun.* **2011**, *47*, 9507–9509. [CrossRef]
74. Wang, H.; Zhang, L.; Chen, Z.; Hu, J.; Li, S.; Wang, Z.; Liu, J.; Wang, X. Semiconductor heterojunction photocatalysts: Design, construction, and photocatalytic performances. *Chem. Soc. Rev.* **2014**, *43*, 5234–5244. [CrossRef]
75. Wang, Y.; Wang, Q.; Zhan, X.; Wang, F.; Safdar, M.; He, J. Visible light driven type II heterostructures and their enhanced photocatalysis properties: A review. *Nanoscale* **2013**, *5*, 8326–8339. [CrossRef]
76. Cheng, N.; Tian, J.; Liu, Q.; Ge, C.; Qusti, A.H.; Asiri, A.M.; Al-Youbi, A.O.; Sun, X. Au-Nanoparticle-Loaded Graphitic Carbon Nitride Nanosheets: Green Photocatalytic Synthesis and Application toward the Degradation of Organic Pollutants. *ACS Appl. Mater. Interfaces* **2013**, *5*, 6815–6819. [CrossRef] [PubMed]
77. Yang, Q.; Wang, T.; Zheng, Z.; Xing, B.; Li, C.; Li, B. Constructing interfacial active sites in Ru/g-C_3N_4-x photocatalyst for boosting H_2 evolution coupled with selective benzyl-alcohol oxidation. *Appl. Catal. B Environ.* **2022**, *315*, 121575. [CrossRef]
78. Tan, Y.; Shu, Z.; Zhou, J.; Li, T.; Wang, W.; Zhao, Z. One-step synthesis of nanostructured g-C_3N_4/TiO_2 composite for highly enhanced visible-light photocatalytic H-2 evolution. *Appl. Catal. B Environ.* **2018**, *230*, 260–268. [CrossRef]
79. Chai, B.; Liao, X.; Song, F.; Zhou, H. Fullerene modified C_3N_4 composites with enhanced photocatalytic activity under visible light irradiation. *Dalton Trans.* **2014**, *43*, 982–989. [CrossRef]
80. Bai, X.; Wang, L.; Wang, Y.; Yao, W.; Zhu, Y. Enhanced oxidation ability of g-C_3N_4 photocatalyst via C-60 modification. *Appl. Catal. B Environ.* **2014**, *152*, 262–270. [CrossRef]
81. Xiang, Q.; Yu, J.; Jaroniec, M. Preparation and Enhanced Visible-Light Photocatalytic H-2-Production Activity of Graphene/C_3N_4 Composites. *J. Phys. Chem. C* **2011**, *115*, 7355–7363. [CrossRef]
82. Li, Y.; Zhang, H.; Liu, P.; Wang, D.; Li, Y.; Zhao, H. Cross-Linked g-C_3N_4/rGO Nanocomposites with Tunable Band Structure and Enhanced Visible Light Photocatalytic Activity. *Small* **2013**, *9*, 3336–3344. [CrossRef]
83. Ge, L.; Han, C.; Liu, J. Novel visible light-induced g-C_3N_4/Bi2WO6 composite photocatalysts for efficient degradation of methyl orange. *Appl. Catal. B Environ.* **2011**, *108*, 100–107. [CrossRef]
84. Li, C.; Wang, S.; Wang, T.; Wei, Y.; Zhang, P.; Gong, J. Monoclinic Porous $BiVO_4$ Networks Decorated by Discrete g-C_3N_4 Nano-Islands with Tunable Coverage for Highly Efficient Photocatalysis. *Small* **2014**, *10*, 2783–2790. [CrossRef]
85. Ye, L.; Chen, S. Fabrication and high visible-light-driven photocurrent response of g-C_3N_4 film: The role of thiourea. *Appl. Surf. Sci.* **2016**, *389*, 1076–1083. [CrossRef]
86. Cai, J.; Huang, J.; Wang, S.; Iocozzia, J.; Sun, Z.; Sun, J.; Yang, Y.; Lai, Y.; Lin, Z. Crafting Mussel-Inspired Metal Nanoparticle-Decorated Ultrathin Graphitic Carbon Nitride for the Degradation of Chemical Pollutants and Production of Chemical Resources. *Adv. Mater.* **2019**, *31*, e1806314. [CrossRef] [PubMed]
87. Wu, C.; Teng, Z.; Yang, C.; Chen, F.; Bin Yang, H.; Wang, L.; Xu, H.; Liu, B.; Zheng, G.; Han, Q. Polarization Engineering of Covalent Triazine Frameworks for Highly Efficient Photosynthesis of Hydrogen Peroxide from Molecular Oxygen and Water. *Adv. Mater.* **2022**, *34*, e2110266. [CrossRef] [PubMed]
88. Zhang, Z.; Zhu, Y.; Chen, X.; Zhang, H.; Wang, J. A Full-Spectrum Metal-Free Porphyrin Supramolecular Photocatalyst for Dual Functions of Highly Efficient Hydrogen and Oxygen Evolution. *Adv. Mater.* **2019**, *31*, e1806626. [CrossRef] [PubMed]
89. Hou, H.; Zeng, X.; Zhang, X. Production of Hydrogen Peroxide by Photocatalytic Processes. *Angew. Chem. Int. Ed.* **2020**, *59*, 17356–17376. [CrossRef]
90. Liu, C.; Feng, Y.; Han, Z.; Sun, Y.; Wang, X.; Zhang, Q.; Zou, Z. Z-scheme N-doped $K_4Nb_6O_{17}$/g-C_3N_4 heterojunction with superior visible-light-driven photocatalytic activity for organic pollutant removal and hydrogen production. *Chin. J. Catal.* **2021**, *42*, 164–174. [CrossRef]
91. Li, X.; Xiong, J.; Gao, X.; Huang, J.; Feng, Z.; Chen, Z.; Zhu, Y. Recent advances in 3D g-C_3N_4 composite photocatalysts for photocatalytic water splitting, degradation of pollutants and CO_2 reduction. *J. Alloys Compd.* **2019**, *802*, 196–209. [CrossRef]
92. Ji, C.; Yin, S.-N.; Sun, S.; Yang, S. An in situ mediator-free route to fabricate Cu_2O/g-C_3N_4 type-II heterojunctions for enhanced visible-light photocatalytic H-2 generation. *Appl. Surf. Sci.* **2018**, *434*, 1224–1231. [CrossRef]
93. Wang, J.; Wang, G.; Wang, X.; Wu, Y.; Su, Y.; Tang, H. 3D/2D direct Z-scheme heterojunctions of hierarchical TiO_2 microflowers/g-C_3N_4 nanosheets with enhanced charge carrier separation for photocatalytic H-2 evolution. *Carbon* **2019**, *149*, 618–626. [CrossRef]
94. Wang, W.; Zhang, H.; Chen, Y.; Shi, H. Efficient Degradation of Tetracycline via Coupling of Photocatalysis and Photo-Fenton Processes over a 2D/2D alpha-Fe_2O_3/g-C_3N_4 S-Scheme Heterojunction Catalyst. *Acta Phys. Chim. Sin.* **2022**, *38*, 2201008. [CrossRef]
95. Jia, X.; Hu, C.; Sun, H.; Cao, J.; Lin, H.; Li, X.; Chen, S. A dual defect co-modified S-scheme heterojunction for boosting photocatalytic CO_2 reduction coupled with tetracycline oxidation. *Appl. Catal. B Environ.* **2023**, *324*, 122232. [CrossRef]
96. Miao, Z.; Wang, Q.; Zhang, Y.; Meng, L.; Wang, X. In situ construction of S-scheme AgBr/BiOBr heterojunction with surface oxygen vacancy for boosting photocatalytic CO_2 reduction with H_2O. *Appl. Catal. B-Environ.* **2022**, *301*, 120802. [CrossRef]

97. Cao, S.-W.; Liu, X.-F.; Yuan, Y.-P.; Zhang, Z.-Y.; Liao, Y.-S.; Fang, J.; Loo, S.C.J.; Sum, T.C.; Xue, C. Solar-to-fuels conversion over In_2O_3/g-C_3N_4 hybrid photocatalysts. *Appl. Catal. B Environ.* **2014**, *147*, 940–946. [CrossRef]
98. Li, M.; Zhang, L.; Fan, X.; Wu, M.; Wang, M.; Cheng, R.; Zhang, L.; Yao, H.; Shi, J. Core-shell $LaPO_4$/g-C_3N_4 nanowires for highly active and selective CO_2 reduction. *Appl. Catal. B Environ.* **2017**, *201*, 629–635. [CrossRef]
99. Chiu, Y.-H.; Chang, T.-F.M.; Chen, C.-Y.; Sone, M.; Hsu, Y.-J. Mechanistic Insights into Photodegradation of Organic Dyes Using Heterostructure Photocatalysts. *Catalysts* **2019**, *9*, 430. [CrossRef]
100. Wei, X.; Wang, X.; Pu, Y.; Liu, A.; Chen, C.; Zou, W.; Zheng, Y.; Huang, J.; Zhang, Y.; Yang, Y.; et al. Facile ball-milling synthesis of CeO_2/g-C_3N_4 Z-scheme heterojunction for synergistic adsorption and photodegradation of methylene blue: Characteristics, kinetics, models, and mechanisms. *Chem. Eng. J.* **2021**, *420*, 127719. [CrossRef]
101. Li, M.-F.; Liu, Y.-G.; Zeng, G.-M.; Liu, N.; Liu, S.-B. Graphene and graphene-based nanocomposites used for antibiotics removal in water treatment: A review. *Chemosphere* **2019**, *226*, 360–380. [CrossRef] [PubMed]
102. Thanh Binh, N.; Huang, C.P.; Doong, R.-a. Photocatalytic degradation of bisphenol A over a $ZnFe_2O_4$/TiO_2 nanocomposite under visible light. *Sci. Total Environ.* **2019**, *646*, 745–756. [CrossRef]
103. Khan, I.; Saeed, K.; Zekker, I.; Zhang, B.; Hendi, A.H.; Ahmad, A.; Ahmad, S.; Zada, N.; Ahmad, H.; Shah, L.A.; et al. Review on Methylene Blue: Its Properties, Uses, Toxicity and Photodegradation. *Water* **2022**, *14*, 242. [CrossRef]
104. Guo, Z.; Kodikara, D.; Albi, L.S.; Hatano, Y.; Chen, G.; Yoshimura, C.; Wang, J. Photodegradation of organic micropollutants in aquatic environment: Importance, factors and processes. *Water Res.* **2023**, *231*, 118236. [CrossRef]
105. Liu, C.; Dai, H.; Tan, C.; Pan, Q.; Hu, F.; Peng, X. Photo-Fenton degradation of tetracycline over Z-scheme Fe-g-C_3N_4/Bi_2WO_6 heterojunctions: Mechanism insight, degradation pathways and DFT calculation. *Appl. Catal. B Environ.* **2022**, *310*, 121326. [CrossRef]
106. Peng, X.; Wu, J.; Zhao, Z.; Wang, X.; Dai, H.; Wei, Y.; Xu, G.; Hu, F. Activation of peroxymonosulfate by single atom Co-N-C catalysts for high-efficient removal of chloroquine phosphate via non-radical pathways: Electron-transfer mechanism. *Chem. Eng. J.* **2022**, *429*, 132245. [CrossRef]
107. Baladi, E.; Davar, F.; Hojjati-Najafabadi, A. Synthesis and characterization of g-C_3N_4-$CoFe_2O_4$-ZnO magnetic nanocomposites for enhancing photocatalytic activity with visible light for degradation of penicillin G antibiotic. *Environ. Res.* **2022**, *215*, 114270. [CrossRef]
108. Ghosh, U.; Pal, A. Fabrication of a novel Bi_2O_3 nanoparticle impregnated nitrogen vacant 2D g-C_3N_4 nanosheet Z scheme photocatalyst for improved degradation of methylene blue dye under LED light illumination. *Appl. Surf. Sci.* **2020**, *507*, 144965. [CrossRef]
109. Jin, Z.; Hu, R.; Wang, H.; Hu, J.; Ren, T. One-step impregnation method to prepare direct Z-scheme $LaCoO_3$/g-C_3N_4 heterojunction photocatalysts for phenol degradation under visible light. *Appl. Surf. Sci.* **2019**, *491*, 432–442. [CrossRef]
110. Song, R.; Yao, L.; Sun, C.; Yu, D.; Lin, H.; Li, G.; Lian, Z.; Zhuang, S.; Zhang, D. Electrospun Membranes Anchored with g-C_3N_4/MoS_2 for Highly Efficient Photocatalytic Degradation of Aflatoxin B-1 under Visible Light. *Toxins* **2023**, *15*, 133. [CrossRef]
111. Song, R.; Kang, S.; Yao, L.; Zheng, L.; Yu, D.; Zhang, D. Construction of an La-$BiVO_4$/O-Doped g-C_3N_4 Heterojunction Photocatalyst Embedded in Electrospinning Nanofibers. *Langmuir* **2023**, *39*, 6647–6656. [CrossRef] [PubMed]
112. Li, Y.; Wang, J.; Yang, Y.; Zhang, Y.; He, D.; An, Q.; Cao, G. Seed-induced growing various TiO_2 nanostructures on g-C_3N_4 nanosheets with much enhanced photocatalytic activity under visible light. *J. Hazard. Mater.* **2015**, *292*, 79–89. [CrossRef] [PubMed]
113. Zhang, W.; Sun, Y.; Dong, F.; Zhang, W.; Duan, S.; Zhang, Q. Facile synthesis of organic inorganic layered nanojunctions of g-C_3N_4/(BiO_2CO_3 as efficient visible light photocatalystt. *Dalton Trans.* **2014**, *43*, 12026–12036. [CrossRef]
114. Hong, Y.; Jiang, Y.; Li, C.; Fan, W.; Yan, X.; Yan, M.; Shi, W. In-situ synthesis of direct solid-state Z-scheme V_2O_5/g-C_3N_4 heterojunctions with enhanced visible light efficiency in photocatalytic degradation of pollutants. *Appl. Catal. B Environ.* **2016**, *180*, 663–673. [CrossRef]
115. Zhou, L.; Zhang, W.; Chen, L.; Deng, H. Z-scheme mechanism of photogenerated carriers for hybrid photocatalyst Ag_3PO_4/g-C_3N_4 in degradation of sulfamethoxazole. *J. Colloid Interface Sci.* **2017**, *487*, 410–417. [CrossRef]
116. Tian, Y.; Ge, L.; Wang, K.; Chai, Y. Synthesis of novel MoS_2/g-C_3N_4 heterojunction photocatalysts with enhanced hydrogen evolution activity. *Mater. Charact.* **2014**, *87*, 70–73. [CrossRef]
117. Ye, R.; Fang, H.; Zheng, Y.-Z.; Li, N.; Wang, Y.; Tao, X. Fabrication of $CoTiO_3$/g-C_3N_4 Hybrid Photocatalysts with Enhanced H_2 Evolution: Z-Scheme Photocatalytic Mechanism Insight. *ACS Appl. Mater. Interfaces* **2016**, *8*, 13879–13889. [CrossRef] [PubMed]
118. Wang, M.; Shen, M.; Zhang, L.; Tian, J.; Jin, X.; Zhou, Y.; Shi, J. 2D-2D MnO_2/g-C_3N_4 heterojunction photocatalyst: In situ synthesis and enhanced CO_2 reduction activity. *Carbon* **2017**, *120*, 23–31. [CrossRef]
119. Yuan, Y.-P.; Cao, S.-W.; Liao, Y.-S.; Yin, L.-S.; Xue, C. Red phosphor/g-C_3N_4 heterojunction with enhanced photocatalytic activities for solar fuels production. *Appl. Catal. B Environ.* **2013**, *140*, 164–168. [CrossRef]